PROBING INTERFACIAL PROCESSES ON CARBON NANOTUBES AND GRAPHENE SURFACES

A THESIS

SUBMITTED TO THE DEPARTMENT OF PHYSICS

AND THE GRADUATE SCHOOL OF ENGINEERING AND SCIENCE

OF BILKENT UNIVERSITY

IN PARTIAL FULFILLMENT OF THE REQUIREMENTS

FOR THE DEGREE OF

MASTER OF SCIENCE

By

Nurbek Kakenov

August, 2012

I certify that I have read this thesis and that in my opinion it is fully adequate, in scope and in quality, as a thesis for the degree of Master of Science.

Asst. Prof. Dr. Coşkun Kocabaş

I certify that I have read this thesis and that in my opinion it is fully adequate, in scope and in quality, as a thesis for the degree of Master of Science.

Prof. Dr. Oğuz Gülseren

I certify that I have read this thesis and that in my opinion it is fully adequate, in scope and in quality, as a thesis for the degree of Master of Science.

Prof. Dr. Raşit Turan

Approved for the Graduate School of Engineering and Science:

Prof. Dr. Levent Onural
Director of the Graduate School

ABSTRACT

PROBING INTERFACIAL PROCESSES ON CARBON NANOTUBE AND GRAPHENE SURFACES

Nurbek Kakenov
M.S. in Physics
Supervisor: Asst. Prof. Dr. Coşkun Kocabaş
August, 2012

The surface of low-dimensional carbon (carbon nanotubes and graphene) has unique electronic properties due to the delocalized p-orbitals. Very high carrier mobility with nanoscale dimension make carbon nanotubes and graphene promising candidates for high performance electronics. Besides electronic properties, the delocalized orbitals have a strong tendency to adsorb aromatic molecules via p-electronic interactions. The strong non-covalent interactions between the graphitic surface and organic molecules provide a unique template for supramolecular chemistry and sensing applications. A comprehensive understanding of these forces at atomic and molecular level still remains a challenge. In this thesis, we have used carbon nanotube networks and graphene as model systems to understand molecular interactions on carbon surface. We have developed processes to integrate these model materials with sensitive and surface specific sensors, such as surface plasmon sensor and quartz crystal microbalance. In the first part of the thesis, we integrated surface plasmon resonance (SPR) sensors with networks of single-walled carbon nanotubes to study interactions between SWNT and organic molecules. In the second part, we probe interfacial processes on graphene surface by mass detection. We anticipate that the developed methods could provide a sensitive means of detecting fundamental interaction on carbon surfaces.

Keywords: binding parameter, carbon nanotube, chemical adsorption, CVD, graphene, quartz crystal microbalance, surface plasmon resonance sensor.

ÖZET

KARBON NANOTÜP VE GRAFEN YÜZEYLERİNDEKİ ARA-YÜZEYSEL ETKİLEŞMELERİN SONDALAMASI

Nurbek Kakenov
Fizik, Yüksek Lisans
Tez Yöneticisi: Asst. Prof. Dr. Coşkun Kocabaş
Ağustos, 2012

Düşük boyutlu karbon (nanotüpler ve grafen) yüzeyi delokalize p-orbital ile sıradışı elektronik özellikler gostermektedir. Nanometre boyutu ile birlikte çok yüksek elektron hareketliliğine sahip olan karbon nanotüpler ve grafen yüksek performanslı elektronik alanında umut verici adaylar olarak belirtiliyolar. Benzersiz elektronik özelliklerinin yanı sıra, delokalize p-orbital etkileşim yoluyla aromatik moleküllerin güçlü emilme eğilimi vardır. Grafitik yüzey ve organik molekülleri arasındaki güçlü etkileşimler supramoleküler kimya ve bioalgılama uygulamaları için yeni bir platform sunmaktadır. Bu etkileşimlerin mekanizmaları atomik ve moleküler seviyede kapsamlı bir şekilde anlaşılamamıştır. Bu etkileşmeleri anlamak için yüksek duyarlılıga sahip yeni teknikler ile düşük boyutlu karbon yüzey üzerindeki organik moleküllerin dinamiğini araştırma ihtiyacı bulunmaktadır. Bu tezde, karbon yüzey üzerindeki moleküler etkileşimleri anlamak için model sistemler olarak karbon nanotüp ağları ve grafen kullanmıştır. Biz yüzey plazmon sensörü ve kuvartz kristal mikroterazi gibi hassas ve yüzeye özel sensörler ile bu model malzemeleri entegre yollarını geliştirdik. Tezin ilk bölümünde tek duvarlı karbon nanotüp rin ağlarını yüzey plazmon rezonans sensörlerini kullanarak karbon nanotüp ve organik moleküllerin arasındaki etkileşimleri inceledik. İkinci bölümde ise, grafen yüzeyindeki ektileşimleri kütle ölçümü ile araştırdık.

Anahtar sözcükler: bağlanma parametresi, karbon nanotüp, kimyasal adsopsiyon, CVD, grafen, yüzey plasmon resonans, kuvartz kristal mikroterazi.

Acknowledgement

I express my most sincere gratitude and appreciation to Asst. Prof. Dr. Coşkun Kocabaş. Not only his guidance and support have always leaded me, but also motivated me during the whole time of my research work. Without his instructions and supportive attitude, this thesis would not have been possible.

I as well present my gratitude to Prof. Dr. Oğuz Gülseren and Prof. Dr. Raşit Turan for their judgments and helpful critics as the Master's Thesis committee.

I also would like to thank all the Kocabaş group and ARL members for providing wonderful atmosphere during the course of two years.
Above all, I am grateful to Osman Balcı for his support, guidance, and mentorship throughout the years I have spent in Bilkent.

I am indebted to Şerafettin Küçükoğlu my chemistry teacher, for helping me build the very first steps of my scientific endeavor.

Most of all I am thankful to Özlem Yavaş for always being supportive, caring, and joyful. Her cheerful attitude and her being always by my side could not have made the days of studying much easier, enjoying, and entertaining.

I owe my profound gratitude to my family. Without their love and care it would not have been possible to do any of this, and without them nothing I do would matter. And I dedicate this thesis work to my beloved grandmother Shaken Seylakunova with whom I associate all the good things that our family has.

Contents

1. Introduction 1

1.1 Carbon Based Nanomaterials 1

1.2 Organization of the thesis 2

2. Molecular interactions on carbon surfaces 4

3. Properties and Synthesis of SWNT and Graphene 8

3.1 Single Wall Carbon Nanotubes 8

3.2 Graphene 13

3.3 Synthesis of Single Wall Carbon Nanotubes 17
3.3.1 Arc discharge evaporation method 17
3.3.2 Laser ablation method 18
3.3.3 High-pressure carbon monoxide method 19
3.3.4 Chemical vapor deposition method 20

3.4 Synthesis of graphene 25
3.4.1 Mechanical exfoliation 25
3.4.2 Thermal decomposition of SiC 26
3.4.3 Chemical vapor deposition synthesis of graphene 26

4. Probing Molecular Interactions on Carbon Nanotube Surfaces 32

4.1 Surface plasmon polariton 32

5. Probing Interfacial Processes on Graphene 47

5.1 Interfacial mass detection with piezoelectric transducers 47

5.2 Integration of graphene with QCM 49

6. Summary and future work 60

7. Bibliography: 62

List of Figures

Figure 3-1 Schematic representation of the honeycomb lattice. The chiral vector $\boldsymbol{Ch = na1 + ma2}$ is a combination of unit vectors, $\boldsymbol{a1}$ and $\boldsymbol{a2}$ and specified by the chiral angle θ. At zigzag line chiral angle is defined to be zero. $OBCA$ defines typical 1D unit cell for SWNTs, $\boldsymbol{T}$ lattice vector. 10

Figure 3-2 (a) Tight-binding band diagram of single sheet graphite plane. (b) Allowed k-vectors of the (4, 4) and (5, 0) indexed tubes (brown lines). Note that the (4, 4) is metallic the line cross Dirac points, whereas the (5, 0) is semiconducting tube the lines do not cross Dirac points. *Figures were adapted from mathematica simulations developed by Jessica Alfonsi (University of Pandova, Italy)*..... 11

Figure 3-3 Diagram for possible combinations of indices (n, m) including armchair, zigzag and chiral types of carbon nanotubes. All armchair SWNTs are defined to be metallic whereas, only some combinations of zigzag behave like metals.12

Figure 3-4 (a) Honeycomb lattice structure and (b) Brillouin zone. $\boldsymbol{a1}$ and $\boldsymbol{a2}$ are the primitive unit vectors. The corner points are called as Dirac points K and K'.. 14

Figure 3-5 (a) Brillouin Zone honeycomb structure. (b) Graphene band structure. The points where π and π^* bands match are at Dirac points. The conduction and valence bands touch at Dirac points indicating semimetallic behavior of graphene. The ambipolar property indicates that either electron or hole can be the charge carrier long the graphene plane. *The figures were adapted from mathematica simulation developed by Vladimir Gavryushin (Vilnius University, Lithuania)* 16

Figure 3-6 Schematic of arc-discharge evaporation method. High current is applied to graphite electrodes in ambient He gas. 18

Figure 3-7 Schematics for laser ablation method. High power pulses are incident on graphite source while maintaining ambient temperature at 1200℃. 19
Figure 3-8 Schematics for CVD technique. Hydrocarbons, feedstock of carbon atoms, decompose by catalyst particles at elevated temperatures. 20
Figure 3-9 CVD system equipment for SWNT growth. CVD system contains (a) furnace with inside quartz silica tube vacuum chamber system, (b) gas flow control units and (c) the sample close-up inside furnace. (d) SEM image of SWNT network. 23
Figure 3-10 Raman spectrum of single wall carbon nanotube. D- and G' bands indicate disorders whiles G-band carries graphitic nature. 24
Figure 3-11 SWNT transfer-print process on gold metal surface step diagram. 25
Figure 3-12 CVD system equipment for graphene growth. CVD equipment includes (a) gas flow control units, (b) sample close-up inside furnace, (c) furnace and inside quartz silica tube integrated with vacuum chamber system. 29
Figure 3-13 Raman and transmission spectra of graphene layers grown on Cu foil. (a) Raman spectrum of single layer graphene. (b) Raman spectra of mono-, bi-, and trilayers of graphene and (c) graphene on copper and transferred graphene. (d) Absorption spectra of number of graphene on quartz substrate. 30
Figure 3-14 Schematics for transfer-print procedure of graphene sheet on quartz crystal surface. 31
Figure 4-1 Dispersion curve of surface plasmon polaritons at at metal/air and metal/glass interfaces. Light line in prism is tilted enabling momentum energy match for SPP excitations. The plasmons at the metal/glass interface cannot be excited since the dispersion curve is out of light cone. 33
Figure 4-2 Surface plasmon polariton excitation geometries. a) Kretschmann configuration b) Otto configuration. 35
Figure 4-3 Transfer printing process of SWNT network grown on SiO_2 coated Si substrates. 36
Figure 4-4 Electron micrographs of SWNT networks with various tube densities grown by chemical vapor deposition on SiO_2 substrates. Tube density was controlled by changing the concentration of the catalyst. These networks are named as sub-

monolayer (D1=1 SWNT/μm^2), monolayer (D2=10 SWNT/μm^2) and multilayer (D3=50 SWNT/μm^2), respectively. The tube diameter ranges between 0.7 nm to 4 nm. 38

Figure 4-5 Experimental setup (Kretschmann configuration) used to excite SPP on metal surface coated with SWNT network. The thickness of the gold layer is 50 nm. The prism is mounted on a double rotary state. The reflected beam is detected by a photodiode. The incidence angle and the wavelength of the laser are controlled with a precision of less than 0.01 deg. and 1 nm, respectively. . 40

Figure 4-6 The reflectivity maps (angular dispersion curves) from the SWNT coated gold surface as a function of incidence angle and the excitation wavelength. The light source is TM polarized. As the density of SWNTs network increases, the effective index of the surface plasmon-polaritons increases resulting in a red shift in the plasmon resonance wavelength. The color map shows the scale for the reflectivity. 41

Figure 4-7 (a) Reflection spectra from the gold surface for various tube densities. The incidence angle is 44 deg. There are two resonances in the reflectivity spectra; bulk plasmon resonance of around 450 nm and surface plasmon resonance of around 600 nm. (b) Reflectivity of the surface as a function of incidence angle for various surface coverage. (c,d) Dependence of surface plasmon resonance wavelength and angle on the surface coverage of SWNT networks, respectively. 43

Figure 4-8 (a) Schematic representation of the microfluidic device integrated with SPR sensor functionalized with SWNT network. The flow chamber is sealed on SWNT coated gold surface. The glass slide is attached on the prism using an index matching fluid. (b) Reflectivity of the gold surface as a function of incidence angle at 635 nm. The resonance angle is 57 deg. (c) Time trace of SPR signal for binding interaction of BSA on gold surface coated with various SWNT network. The concentration of BSA is 100 nm. (d) The extracted parameter (β) quantifies the available binding sites on the surface of SPR sensor. The β-parameter for gold and submonolayer SWNT networks is around 0.35. As the density of SWNT increases the β-parameter changes from 0.35 to

0.8 while the association constant stays constant with a value of $0.56x10^5$ M^{-1} sec^{-1}. 45

Figure 5-1 Transfer-printing process of graphene on the front electrode of a quartz crystal microbalance. 50

Figure 5-2 (a) Experimental set-up used for probing resonance characteristic of the QCM. A two-port network analyzer is used to measure scattering parameters. (b) Magnitude (blue lines) and phase (red lines) of the measured scattering parameter S_{11} of the port-1, as a function of frequency for blank (solid line) and graphene coated QCM (dot line). The resonance frequency is 5,007,323.4 Hz. The Q-factor of the resonator is around 22600. After coating the surface of QCM with 0.64 cm^2 graphene, we observed around 20 Hz shift in the resonance frequency. 52

Figure 5-3 Magnitude (a) and phase (b) of scattering parameters measured for QCM coated with multilayer graphene. (c) Measured frequency shift as a function of number of graphene layers. The frequency shift shows a linear dependence on the graphene layers. (d) The bandwidth of the QCM vs. number of graphene layers. 55

Figure 5-4(a) Schematics of the experimental setup used to probe the time trace of the resonance frequency of the QCM. (b) Overlaid time trace of resonance frequency indicating the binding kinetics of Bovine serum albumin (BSA) proteins on the bare QCM surface and graphene coated QCM surface. The concentration of BSA is 100nM. 57

Figure 5-5 Probing oxidation of graphene by mass detection. (a) Change of the resonant frequency and associated mass uptake of graphene exposed to mild oxygen plasma. (b) Raman spectra of graphene with various exposure times. (c-f) Mass uptake of graphene and correlated with Raman intensity for D, G and 2D bands. 59

To my grandmother

Chapter 1

Introduction

1.1 Carbon Based Nanomaterials

Carbon atoms play an essential role both in our-life-cycle and technology. Their use has been of great importance in many applications. With the discovery of new carbon materials like carbon nanotubes [1] and graphene [2], there has been great efforts [1, 3, 4] to implement their extraordinary properties in various devices. Such nanomaterials possess unique electronic conductance, mechanical strength, optical response, and thermal transport [1, 2] which make them very attractive in biosensing [5] and in many other applications.

The surface of low-dimensional carbon (carbon nanotubes and graphene) has unique electronic properties due to the delocalized p-orbitals. Very high carrier mobility together with nanoscale dimension makes carbon nanotubes and graphene promising candidates for high performance electronics [6-11]. Besides unique electronic properties, the delocalized orbital has a strong tendency to adsorb aromatic molecules via p-electronic interactions. The strong non-covalent interactions between the graphitic surface and organic molecules provide a unique template for supramolecular chemistry [12-14] and sensing applications [15-17]. A comprehensive understanding of these forces at atomic and molecular level still remains a challenge. A great deal of computational [18-21] and experimental effort [14, 17, 20, 22-26] has been done to elucidate these interactions. New techniques with improved sensitivities are needed to probe the dynamics of organic molecules on the surface of low-dimensional carbon.

In the literature, adsorption of molecules on carbon surfaces has been studied extensively. The earlier works are based on bulk measurements using sorption isotherms[27-29] and calorimetric studies[30]. Recently, sensitive techniques have been demonstrated. Schedin et. al.[31] have demonstrated detection of a single molecule adsorbed on graphene surface by tracing changes in the Hall resistivity of graphene. Barone et. al.[32] have demonstrated near-infrared optical sensors based on modulation of emission of SWNT in response to adsorbed biomolecules. Electrical response of SWNTs in transistor geometry was also used for detecting adsorbed molecules [15, 16, 33]. Carbon nanotube based capacitive sensors [34], electrochemical sensors [35], and flow sensors [36] are good examples for methods to detect adsorbed molecules on nanotube surface.

In this thesis we studied interfacial processes on carbon surfaces using two model materials; carbon nanotubes and graphene. We have used surface plasmon sensors (SPR) and quartz crystal microbalance (QCM) to probe interfacial processes on carbon nanotube and graphene surfaces. Both methods are surface-specific and widely used especially in biosensing as well as in chemical and surface studies. Any change in the active medium specifically foreign mass depositions can sensitively be detected by SPR and QCM approaches. Although, two methods employ different basis for detections both are capable of sensing similar quantities of measurand with comparable sensitivities, SPR being more sensitive. The working principle of such techniques surface plasmon resonance (SPR) and quartz crystal microbalance (QCM) are described in the following chapters.

1.2 Organization of the thesis

The primary aim of the thesis is to elucidate interfacial processes on carbon surfaces. We have used carbon nanotube and graphene as model systems to understand molecular interactions on carbon surface. We have developed processes to integrate these model materials with sensitive surface specific sensors, such as surface plasmon sensor and quartz crystal microbalance.

Chapter 1 introduces low-dimensional carbon materials as well as their perspectives on chemical adsorption processes, and viable probing methods.

Chapter 2 reviews the literature on the adsorptions mechanisms of the organic chemicals on surface graphitic carbon.

Chapter 3 presents fundamental properties of carbon nanotubes and graphene. The crystal structure and electronic properties will be discussed. Furthermore, their synthesis methods are described.

Chapter 4 presents a method for probing molecular interaction on single-walled nanotube surfaces using surface plasmon sensor. SWNT networks were synthesized by chemical vapor deposition and transfer-printed on gold surfaces. We studied the excitation of surface plasmon-polaritons on nanotube coated gold surfaces with sub-monolayer, monolayer, and multilayer surface coverage. Integrating the fabricated sensor with a microfluidic device, we were able to obtain binding dynamics of a bovine serum albumin (BSA) protein on SWNT networks with various tube densities. The results reveal the kinetic parameters for nonspecific binding of BSA on SWNT surface for various tube densities.

Chapter 5 presents a method for probing interfacial processes on graphene surface using mass detection. Graphene layers were synthesized by chemical vapor deposition on copper foils and transfer-printed on a quartz crystal microbalance (QCM). Probing the mechanical resonance of the QCM, we were able to measure mass density of single layer graphene. We extended the developed technique to probe binding dynamics of proteins on graphene surface. Furthermore, we monitored oxidation of graphene surface under oxygen plasma by tracing the changes of interfacial mass of the graphene layer.

Chapter 6 provides a summary of the study. Future prospects of this research are also discussed.

Chapter 2

Molecular interactions on carbon surfaces

The mechanism behind the interactions between carbon based nanomaterials and organic chemical are not fully understood. Still there remain issues such as quantitative determination of sorption sites, parameters etc. But extensive work has been conducted to analyze such adsorptions on the surface of carbon nanomaterials. In this chapter we would like to review the literature in this field.

B. Pan and B. Xing have presented a review on the adsorption properties of carbon nanotubes and the parameters which have direct impacts on the binding of organic chemicals to carbon surfaces [24]. In particular, they have claimed that the adsorption mechanisms are highly dependent on heterogeneity and hysteresis of carbon nanotube (CNT) and organic molecules interactions, along with hydrophobic interactions, $\pi - \pi$ bonds, electrostatic interactions, and hydrogen bonds.

According to B. Pan et al. organic molecule adsorption on carbon nanotubes cannot be explained by only one adsorption coefficient due to subsequent errors when forecasting the interaction of CNTs and chemicals. Various models [37-46] have been proposed to specify the adsorption of chemicals on CNT. Authors came up with the two explanations concerning heterogeneous adsorption. That's, high energy adsorption state such as carbon nanotube defects [47], functional groups [22] and regions between CNT bundles [48] are presented as first reason while second one is related to condensation of

absorbates. For instance, surface condensation is a process when first two coverings engage with CNT surface while subsequent ones interact with each other. Similarly, hysteresis, defined as the discrepancy between adsorption and desorption, for adsorption of tiny molecules like methane, ethylene, benzene, butane, PAHs, and atrazine on tubes has been observed. As a result, miscellaneous hysteresis was revealed suggesting different outcomes for certain circumstances. These outcomes directly affect future treatments, for instance, depending on hysteresis CNTs can act both as toxics pollutant collector [49] and like reducer pollutant sinks [50]. Thus, properly perceiving hysteresis structure is crucial in determining CNT applications and risks. Various processes like $\pi - \pi$ stacking of benzene-ring solutions with nanotube surfaces [51, 52] and capillary condensations [53] have been accounted for hysteresis. Moreover, the rearrangement of the adsorbent structures [54], applicable to CNT and organic chemicals adsorption, is another explanation for hysteresis. In fact, $\pi - \pi$ bonding of organic molecules prevented CNT bundle formation, and by so doing caused variations in adsorption and desorption processes. As for the shortage of hysteresis, the lack of CNT bundling is accounted causing no available interstitial places for molecule adsorptions. Based on the study, there occur another multiple mechanisms which act simultaneously. That's, hydrophobic interactions, provided by individual tubes external surface, can cause molecules of protein, naphthalene, acidic herbicides, and streptavidin to be adsorbed on CNT. In case the hydrophobicity is sole effect responsible for the adsorptions then it would be easy to predict the interactions of chemicals with CNTs by considering parameters like K_{OW} (octane water distribution coefficient) or K_{HW} (hexadecane water distribution coefficient). However, this is not completely true. Hydrophobic interaction cannot fully explain the behavior of organic chemical and CNTs. Mainly due to the lack of strong correlation between the hydrophobicity for aromatics and affinity of adsorbents [55], high variation in parameter K_{HW} for organics on CNT and so forth. Other aspects like $\pi - \pi$ interactions, hydrogen bonds, and electrostatic behavior are among simultaneously acting mechanisms. To predict the organic molecule's adsorption on CNTs contributions of individual mechanisms to overall system (adsorption) must be considered since various mechanisms respond differently to ambient conditions. Hence

authors proposed three approaches to disclose the relative contributions of a specific mechanism. Firstly, the hydrophobic effect can be excluded by normalizing the sorption coefficients by K_{HW} thus enabling attention to other mechanism [55]. Next, the adsorption of diverse organic chemicals on a certain type of tubes can be compared which can reveal useful information. Lastly, direct sorption experiments can be run in an environment of organic solvents.

Another essential effect on adsorption process can be accounted for the properties of CNTs. As compared to activated carbon (AC) carbon nanotube has lower surface area ($290 \pm 170 m^2/g$) [56]. Nevertheless, the adsorption of organic molecules on SWNT is higher than that of ACs [57]. This suggests that surface area might not be sole attribute when considering chemicals and CNT interactions. While higher surface areas can have strong adsorption strength [46, 58, 59], it is not the case for molecules with planar structure. Since flat surfaces enable better contact to such molecules [60, 61]. Thus, none of the parameters like diameter, porosity, and surface area could individually explain fully the adsorption characteristics of CNT. Furthermore, morphology of carbon nanotubes suggests that the surface area, interstitial and groove regions within CNT-bundles and inside regions of the tubes are accessible sites for sorption. Outer surface and trench regions are mainly open for adsorptions; however, inner sides are closed due to dimensional restrictions. Nonetheless, some molecules like enzymes with the size 3-5 nm are reported to be adsorbed in the inner pores of tubes [62]. Moreover, these inner pores can be blocked by molecules such as amorphous carbon, functional groups, and catalyst nanoparticles. Lack of bundling of CNTs could be another reason for inaccessible interstitial sites [44] or it might be huge molecules which fail to fit in the sites [63]. Hence the readiness of the site for organic chemical adsorptions on CNTs are greatly relies on the properties of the carbon nanotubes and their accumulations. Another nature, which affects the adsorptions, is the chirality of the tubes. Although, $C - C$ bonds are the same kind in the plane of graphite, it is not the case for zigzag, armchair and chiral types of CNTs varying by length and positions to the axis of tubes [60].

The functional groups like $-OH, -C=O, -COOH$ can be included in CNTs. These groups can alter the surface of carbon nanotubes to be more hydrophilic and fitted for the polar molecule adsorptions [43, 64, 65]. However functional groups may also cause the higher diffusional resistance [66] and reduction of availability and attraction of tubes surfaces [56, 67]. Besides, since there is delocalized π orbit in every atom in CNT this can result in the formation of $\pi - \pi$ bonds [68] between organic molecules, assuming latter contain such π orbit as well. In addition, the polarity and non-polarity of molecules being adsorbed on CNT highly needs different approaches. For instance, polar organic molecules are adsorbed greatly due to high CNT oxygen content. On the other hand, hydrophobic effect the adsorption is low for nonpolar organics within the environment of intensified CNT oxygen content.

As authors report, the SWNTs have shown to be superior to ACs and other adsorbents not only with higher adsorption capacity [41, 43, 69] but with also higher adsorption energy [70], along with the faster equilibrium time [43, 64, 69], and with more efficient regeneration [39, 41]. Similarly SWNTs possess higher adsorption coefficients as compared to ACs. Consequently, SWNT is viable material candidate to be used in air purification and water clearance.

As discussed, many diverse factors determine the interactions between organic chemicals and carbon nanotube affected differently by the ambient conditions. Each mechanism may have different consequences on adsorption process. When H-bond mechanism is superior, for example, the functional groups with higher oxygen content would undergo greater sorption on CNTs, whereas, when hydrophobic behavior is predominant, the affinity and availability of CNT is low for organic chemicals. Thus, it is essential to have greater understanding about the relative contributions of adsorption mechanisms to the entire sorption process.

Chapter 3

Properties and Synthesis of SWNT and Graphene

This chapter presents fundamental properties of carbon nanotubes and graphene. The crystal structure and electronic properties will be discussed. Furthermore, their synthesis methods are described.

3.1 Single Wall Carbon Nanotubes

Carbon nanotubes were discovered by Iijima in 1991 at NEC Laboratory [1]. Following years single-wall carbon nanotubes (SWNTs) were synthesized using the same technique. The structure and properties of SWNT were substantially studied by many scientists stimulated by 1D quantum effects.

SWNT is a cylinder formed from honeycomb crystalline of graphene sheet. The structure of single-wall carbon nanotube is a collection of 1D unit cell defined by the vectors $\boldsymbol{C}_h$ and **T** in figure 3-1. The circumference of any carbon nanotube is expressed in terms of the chiral vector $\boldsymbol{C}_h = n\hat{\boldsymbol{a}}_1 + m\hat{\boldsymbol{a}}_2$ two sides of graphene layer. The formation wholly depends on the pair of integers (n, m), which specify chiral vector, and chiral angle. In fact, chiral angle is defined as the angle between chiral vector and "zigzag" orientation ($\theta = 0$) as depicted in figure 3-1. Theoretically three distinct types of carbon nanotubes can be constructed by rolling up the graphene sheet. If the chiral angles are 0 and 30 degrees it corresponds to zigzag and armchair types respectively, and if the chiral is between to extremes ($0 < \theta < 30$) then it becomes chiral type of the

carbon nanotube. The translational vector, **T,** is the vector perpendicular to chiral vector, and these vectors define the unit cell of 1D lattice (see figure 3-1). For the chiral vector with (n, m) indices zigzag and armchair can be obtained for (n, 0) and (n, n) in (n, m) notation. All other combinations represent chiral geometry. Furthermore, the nanotube diameter, d_t, is represented by

$$d_t = \frac{\sqrt{3}a_{C-C}(m^2 + mn + n^2)}{\pi} = C_h/\pi \tag{3.1}$$

where $C_h = |\boldsymbol{C}_h|$, a_{C-C} is the C_C bond length (1.42 Å), and the chiral angle is given by

$$\theta = \tan^{-1}\left[\frac{\sqrt{3}n}{2m + n}\right] \tag{3.2}$$

The angle of zigzag nanotube (n, 0) would be $\theta = 60$ and armchair nanotube (n, n) would have $\theta = 0$ value, and hence by symmetry the chiral angle can be assigned to $0 \leq \theta \leq 30$ boundary. Both zigzag and armchair are considered as achiral type while chiral type carbon nanotubes have any angle values within boundary except extreme angles 0 and 30. Another significant parameter describing SWNT structure is number of hexagons, N, per unit cell of a chiral nanotube, defined by indices (n, m) is represented in the equation

$$N = 2(m^2 + mn + n^2)/d_R \tag{3.3}$$

where $d_R = 3d$ if $n - m$ is a multiple of $3d$, if $n - m$ is not a multiple of $3d$ $d_R = d$, and d is the largest common divisor of (n, m).

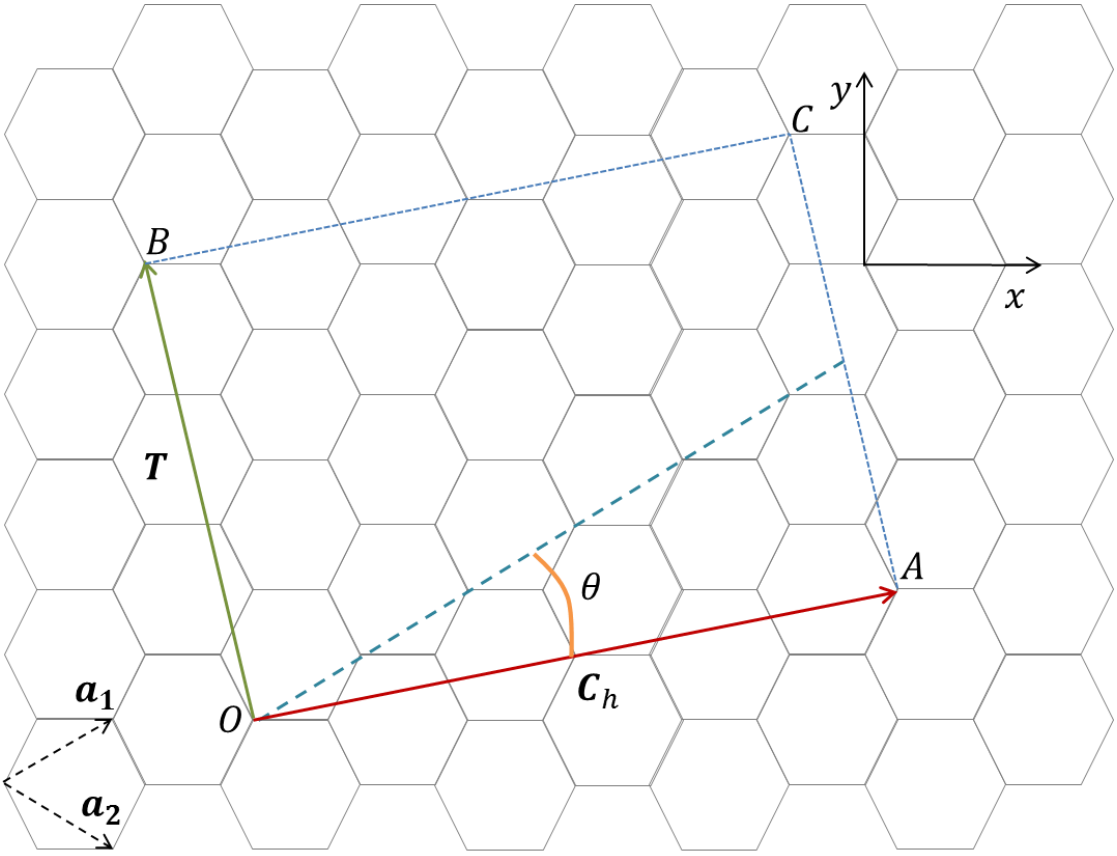

Figure 3-1 Schematic representation of the honeycomb lattice. The chiral vector $\boldsymbol{C_h = n\hat{a}_1 + m\hat{a}_2}$ is a combination of unit vectors, $\boldsymbol{\hat{a}_1}$ and $\boldsymbol{\hat{a}_2}$ and specified by the chiral angle θ. At zigzag line chiral angle is defined to be zero. $OBCA$ defines typical 1D unit cell for SWNTs, $\boldsymbol{T}$ lattice vector.

Studies [71, 72] have shown that geometric structure of carbon nanotubes affects their electronic properties. Despite graphene has zero band gap and considered as semimetal, carbon nanotubes can be classified into metals and semiconductors which highly relies on diameter and helicity of the tubes [73]. Dresselhauss et al. in their study have summarized the band-folding picture by the unique band structure of mono-layer graphite plane, which has only six crossings of Fermi level in k-space, and by the quantization k-momentum of electron along circumferential line [72]. Accordingly, graphene sheet is a zero-band-gap semiconductor, and its electronic structure is given by the occupied π and unoccupied π^* bands. Figure 3-2, depicts K point in the Brillouin zone where linearly dispersed two bands coincide at the Fermi level. There are six such K points at each corner of the honeycomb structure. Periodical boundary

conditions established in circumferential direction, dictate that the allowed **k** states, highly dependent on radius and helicity of carbon nanotubes, in the graphitic plane. If allowed **k** states involve the *K* point, then the structure is metallic two bands possessing linear dispersion at the Fermi level. Also if, the K point is not contained the structure exhibits semiconducting property with various band gaps.

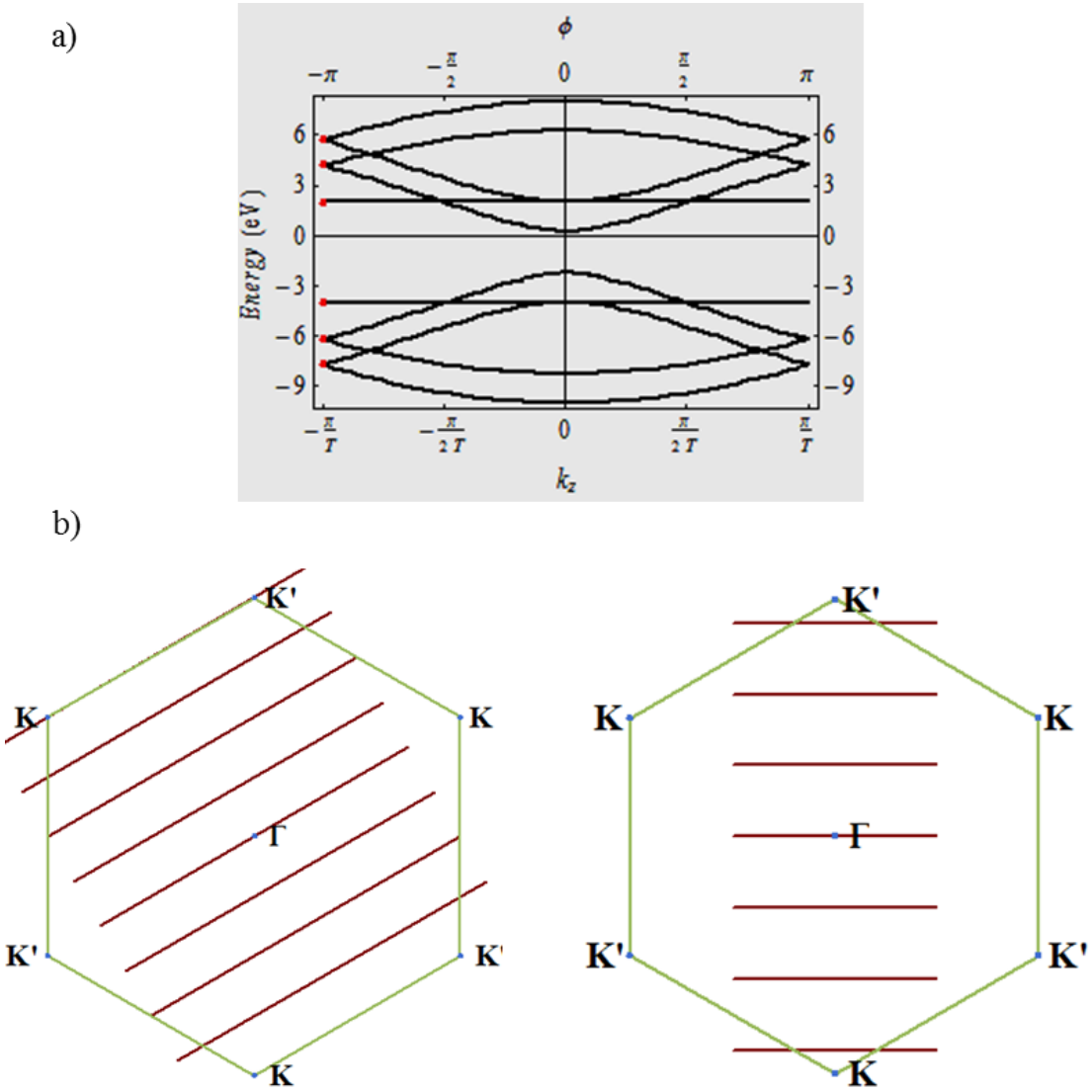

Figure 3-2 (a) Tight-binding band diagram of single sheet graphite plane. (b) Allowed k-vectors of the (4, 4) and (5, 0) indexed tubes (brown lines). Note that the (4, 4) is metallic the line cross Dirac points, whereas the (5, 0) is semiconducting tube the lines do not cross Dirac points. *Figures were adapted from mathematica simulations developed by Jessica Alfonsi (University of Pandova, Italy)*

In fact, chiral indices (n, m) determine the metallic and semiconducting properties of carbon nanotubes. For instance, (n, n) indexed SWNTs are known to be metals; tubes (n, m) are metals if $n - m = 3p$ where p is a nonzero integer at room temperature, and all others ones are semiconductors. The figure 3-3 classifies some combinations of metallic and semiconducting single wall carbon nanotubes.

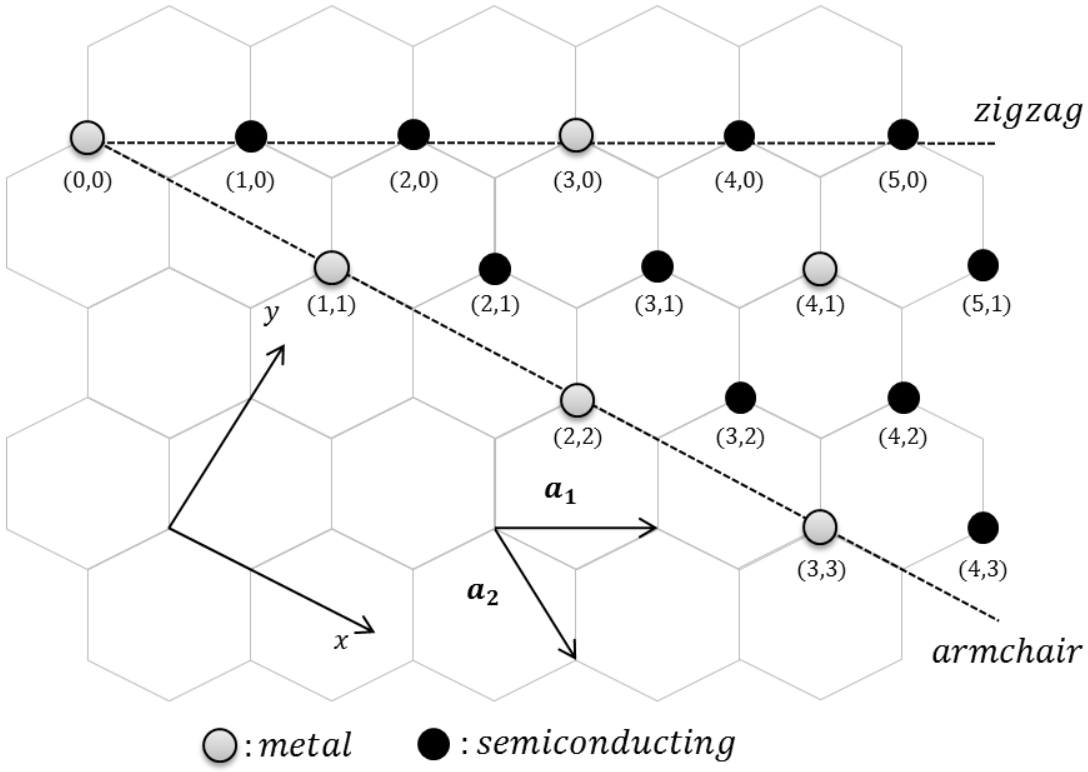

Figure 3-3 Diagram for possible combinations of indices (n, m) including armchair, zigzag and chiral types of carbon nanotubes. All armchair SWNTs are defined to be metallic whereas, only some combinations of zigzag behave like metals.

3.2 Graphene

Graphene is a single atom-thick plane of hexagonally structured and covalently bonded carbon atoms. It exhibits not only high crystal quality but also extraordinary electronic structure. It can be 0D, like buckyballs, 1D like carbon nanotubes and, 3D as such graphite [2], and thus widely used for describing properties of carbon based materials. Since its discovery the structural, electronic, and optical properties have been extensively investigated. Graphene has 2D structure, and previously believed not to exist due to its thermal instability [74]. Nevertheless, graphene has been experimentally manifested [2] and it is stable in the free state due to strong interatomic bonds [75, 76]. One of the most significant characteristics of graphene is its unique electronic property [74]. Electrons propagating through hexagonal lattice totally lose their effective mass leading to waves of electric charge known as quasiparticles described by a Dirac-like equation [2]. These quasiparticles behaving like photons, as though they are massless, still keep their quantum characteristics of quantized charge and spin. What's exciting is that such relativistic particles are governed by quantum electrodynamics offering a ground to test some aspects of it in a more cheap and practical way [77]. Moreover, graphene exhibits ambipolar electric field effect; that's, the charge carriers can be arranged continuously between electrons and holes possessing mobilities as high as 15,000 $cm^2V^{-1}s^{-1}$ under ambient conditions [2, 74]. Furthermore, 2D quantum effect can be observed in graphene sheets. If magnetic field is applied perpendicularly to a current flowing in a 2D plane of graphene, it induces transverse potential difference which increases in discrete steps [2, 74, 78, 79]. This phenomenon is known as Quantum Hall effect (QHE). In metals this effect occurs only at low temperatures whereas in graphene QHE is observed at ambient conditions once again confirming its mono-layer degree.

Carbon, having four valence electrons in its outer orbitals, undergoes sp^2 hybridization in a planar geometry. The s, p_x, p_y orbitals render in-plane σ bonds, z-axis being perpendicular to x-y plane in graphene sheet. Moreover, the robustness of the lattice structure in all allotropes is a result of σ bond. Due to the Pauli principle, these bands have a filled shell which form strong coupling. The unpaired p_z orbital engage with

other neighboring p_z orbitals to create π and π^* bonds in z-axis direction. As the p_z orbital has one electron, the π band is half filled. The figure 3-4 illustrates the lattice structure of graphene. The lattice vectors can be written as $\boldsymbol{a_1} = \frac{a}{2}(3, \sqrt{3})$, $\boldsymbol{a_2} = \frac{a}{2}(3, -\sqrt{3})$, where $a \cong 1.42\text{Å}$ is a carbon-carbon bond length, and the reciprocal lattice vector are given by $\boldsymbol{b_1} = \frac{2\pi}{3a}(1, \sqrt{3})$, $\boldsymbol{b_2} = \frac{2\pi}{3a}(1, -\sqrt{3})$.

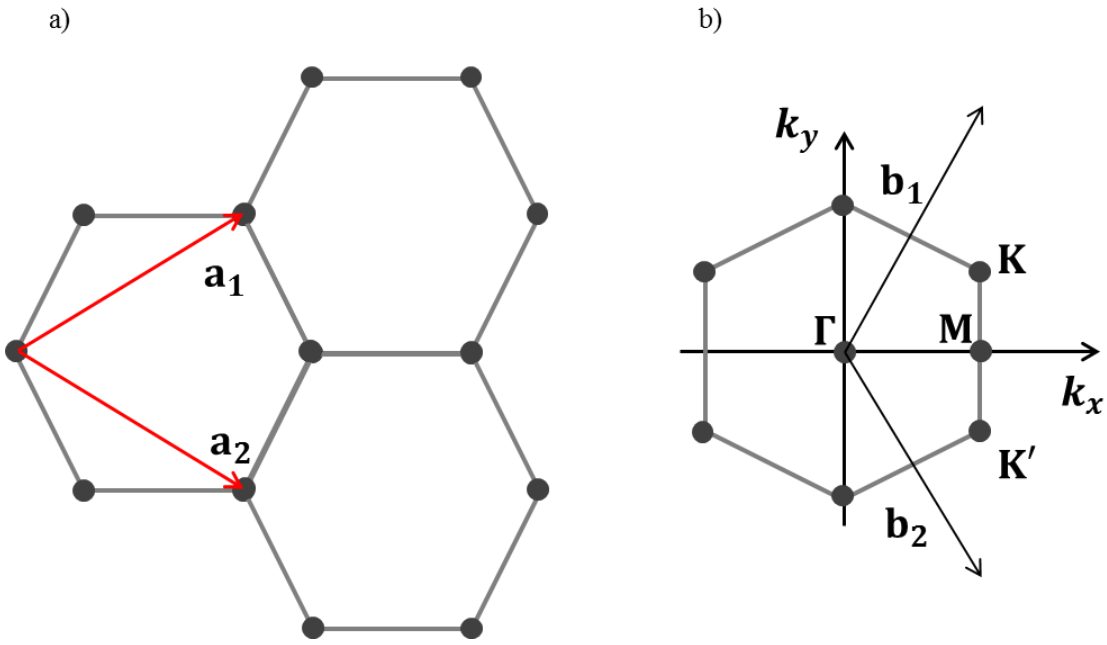

Figure 3-4 (a) Honeycomb lattice structure and (b) Brillouin zone. $\boldsymbol{a_1}$ and $\boldsymbol{a_2}$ are the primitive unit vectors. The corner points are called as Dirac points K and K'.

The two points K *and* K' at the corner of graphene Brillouin zone (BZ) (see figure 3-4b) play significant role in graphene's physics. In momentum space they can be written as $\boldsymbol{K} = \left(\frac{2\pi}{3a}, \frac{2\pi}{3\sqrt{3}a}\right)$, $\boldsymbol{K'} = (\frac{2\pi}{3a}, \frac{2\pi}{-3\sqrt{3}a})$. As mentioned [74], the low-excitations in graphene sheet have been observed to be massless, chiral, and Dirac fermions. The dispersion, valid only at low energies, resembles to massless fermions in quantum electrodynamics except for that fermions in graphene move with speed v_F, 300 times slower than the speed of light [78, 80]. The energy band dispersion for hexagon lattice (see figure 3-5) is expressed by the equation

$$E_{\pm}(k_x, k_y) = \pm\gamma_0 \sqrt{1 + 4\cos\frac{\sqrt{3}k_x a}{2} cos\frac{k_y a}{2} + 4\cos^2\frac{k_y a}{2}} \quad (3.4)$$

where k_x and k_y are x and y components of $\boldsymbol{k}$ momentum vector of electron and γ_0 is the nearest-neighboring hopping energy. In figure 3-5, the energy band of honeycomb lattice structure of graphene is demonstrated. The conduction band and the valence band coincide at discrete points, called K points. Graphene's electronic density of states linearly vanishes with energy at the Dirac point [80]. Thus, neutral graphene is a combination of a metal and a semiconductor, or can be defined as semimetal. It is not a metal since its density of state vanishes and nor semiconductor as there is no band gap in the spectrum, and hence zero energy needed to excite electrons.

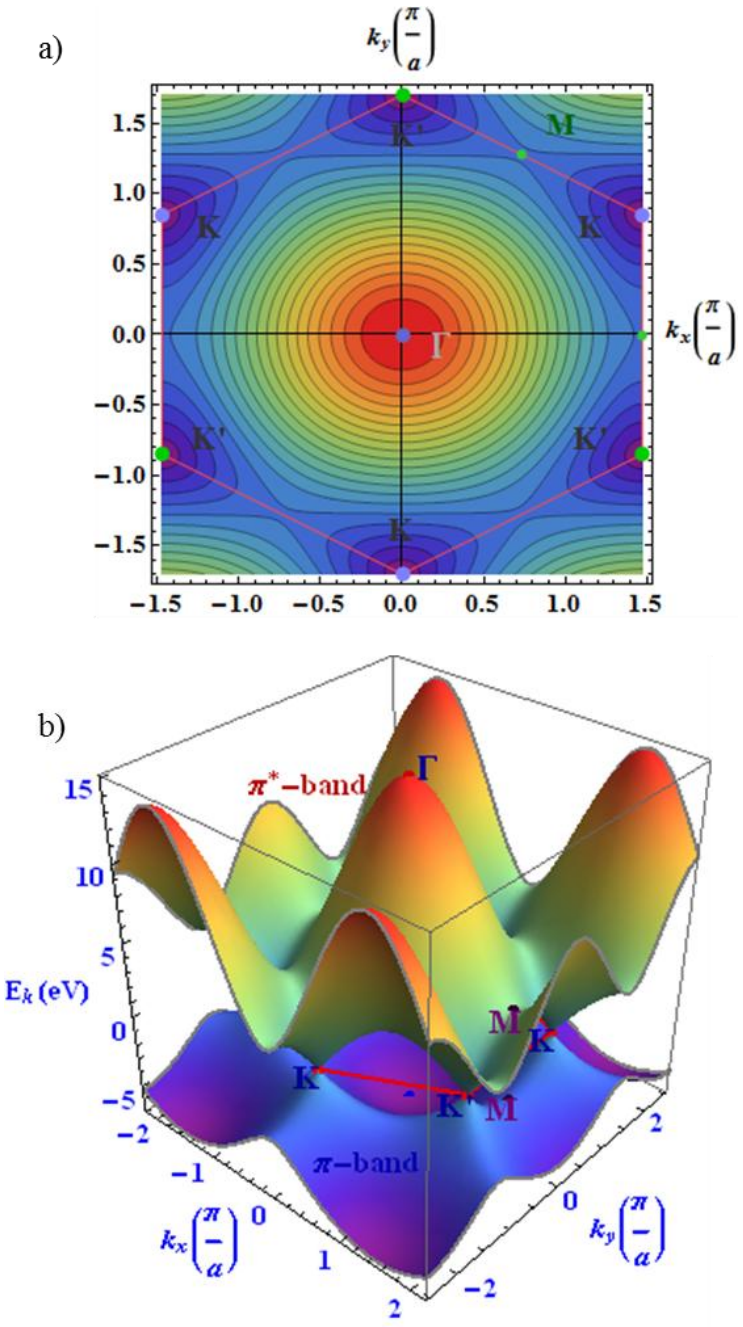

Figure 3-5 (a) Brillouin Zone honeycomb structure. (b) Graphene band structure. The points where $\boldsymbol{\pi}$ and $\boldsymbol{\pi}^*$ bands match are at Dirac points. The conduction and valence bands touch at Dirac points indicating semimetallic behavior of graphene. The ambipolar property indicates that either electron or hole can be the charge carrier long the graphene plane. *The figures were adapted from mathematica simulation developed by Vladimir Gavryushin (Vilnius University, Lithuania)*

3.3 Synthesis of Single Wall Carbon Nanotubes

Since the discovery of carbon nanotubes, many studies have focused on the improvement of synthesis methods. Of them, laser evaporation [81, 82], arc-discharge [1, 81, 83, 84], HiPco [85-87], and chemical vapor deposition (CVD) [81, 84, 88-90] methods have been preferably used to yield high quality carbon nanotube. This section summarizes briefly some techniques and explains in detail chemical vapor deposition technique.

3.3.1 Arc discharge evaporation method

Arc discharge evaporation can produce both single-walled and multi-walled carbon nanotubes amongst other carbon forms. In fact, this is the first method to produce carbon nanotubes [1]. The arc discharge method employs two very close graphite rods connected to DC current. When high current passes through electrodes carbon atoms are ejected from anode and drift toward cathode [91]. Very high temperature ($> 3000℃$) needed to vaporize carbon atoms. These ejected carbon atoms deposit themselves on the surface of cathode in tubular form. Multi-walled carbon nanotubes grown by arc discharge method possess lower defects, and have better electrical, thermal, and mechanical properties. In case when metallic nanoparticles are used as catalysts SWNT can be grown in arc discharge method [1, 81, 83, 84]. The disadvantage of the arc evaporation is that carbon nanotubes must be purified since process contains other graphite crystalline. The basic scheme for arc-discharge system is shown in figure 3-6.

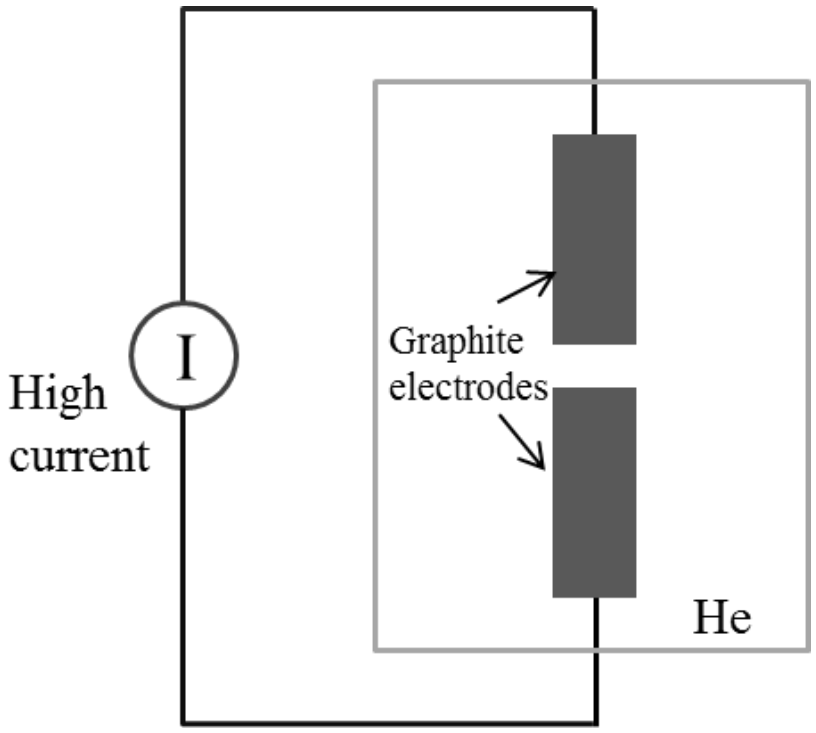

Figure 3-6 Schematic of arc-discharge evaporation method. High current is applied to graphite electrodes in ambient He gas.

3.3.2 Laser ablation method

Laser ablation method is based on vaporizing carbon atoms by laser pulses. A powerful pulsed laser is used to target carbon source in hot gas atmosphere at 1200ºC [81, 82]. To sustain the reliable condition for growth of carbon nanotube double quartz tube is utilized in an oven, where the target is pure graphite in an ambient gas such as Ar. It is crucial to maintain reliable temperature conditions since otherwise no carbon nanotube would grow. The laser targets the graphite causing ejection of carbon atoms, and those atoms are caught by flow reach the substrate where it starts to form multi-walled carbon nanotubes (MWNT). As to generate single-walled carbon nanotubes (SWNT) the metal catalyst are added to graphite target. The catalyst particles functions to keep open fullerenes as the additional carbon atoms attach forming nanotubes. As compared to arc discharge method the nanotubes synthesized by laser ablation are more pure up to %90. There is less by products like amorphous carbon, fullerenes, and graphitic clusters since the growth process is confined spatially supporting conditions more

conductive to nanotube formation. The schematic of laser ablation system is illustrated in figure 3-7.

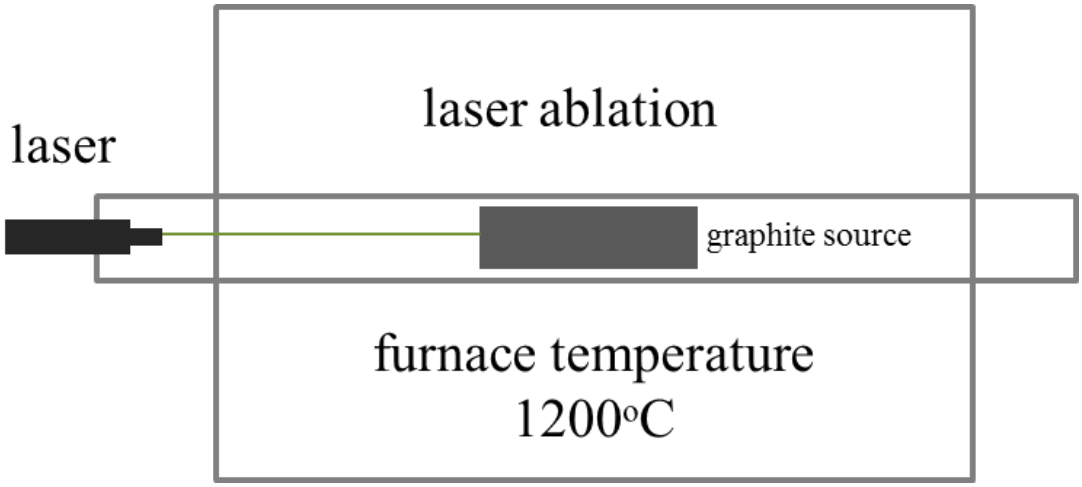

Figure 3-7 Schematics for laser ablation method. High power pulses are incident on graphite source while maintaining ambient temperature at 1200℃.

3.3.3 High-pressure carbon monoxide method

High-pressure Carbon Monoxide (HiPCO) produces carbon nanotubes by decomposing organometallics such as iron pentacarbonyl $Fe(CO)_5$ [92]. At high pressures and elevated temperatures the production of SWNT can be triggered by rotting iron pentacarbonyl in continuously flowing CO [85]. Iron pentacarbonyl functions as the catalytic particles. As $Fe(CO)_5$ is decomposed its products create clusters which become basis for nanotube growth in a gas phase. In this process the carbon is the product of the Boudoard reaction: $CO + CO \rightarrow CO_2 + C(SWNT)$ Hence the mixture of $Fe(CO)_5$ and CO are injected into reactor chamber to be rapidly heated to enhance the formation of carbon nanotubes. The products of this reaction, SWNT and iron particles, are extracted by hot, dense gas flow and CO is removed by filters. The characterizations reveal that the SWNT generated by HiPco method are free of amorphous carbon thus making purification process redundant which is inevitable in arc-discharge and laser ablation methods. The SWNT production can go up several g/day by HiPco method [85].

3.3.4 Chemical vapor deposition method

Since the discovery, the principal methods for the synthesis of carbon nanotubes were arc discharge and laser evaporations of carbon feedstock. Both methods have capability of producing MWNT and SWNT materials. The major issues concerning with these methods are high temperature ($> 3000℃$) necessity for solid carbon evaporations, and undesired by-products such as fullerenes, graphitic polyhedrons with enclosed metal particles, and amorphous carbon which come along with tubular carbon [73]. Hence, nanotube materials need to go through additional procedures to yield pure carbon nanotubes. Since many applications require high quality carbon nanotubes, the growth processes have to be perfected [93]. Significant work has been done to develop defect-free carbon nanotubes growth and chemical vapor deposition (CVD) method is a promising candidate. In this section the SWNT growth is discussed.

The CVD process involves the decomposition of hydrocarbons triggered by catalyst particles at an elevated temperatures and the precipitation of carbon atoms in a tubular form on the surface, dispersed by transition-metals. The figure 3-8 depicts schematic representation of CVD system.

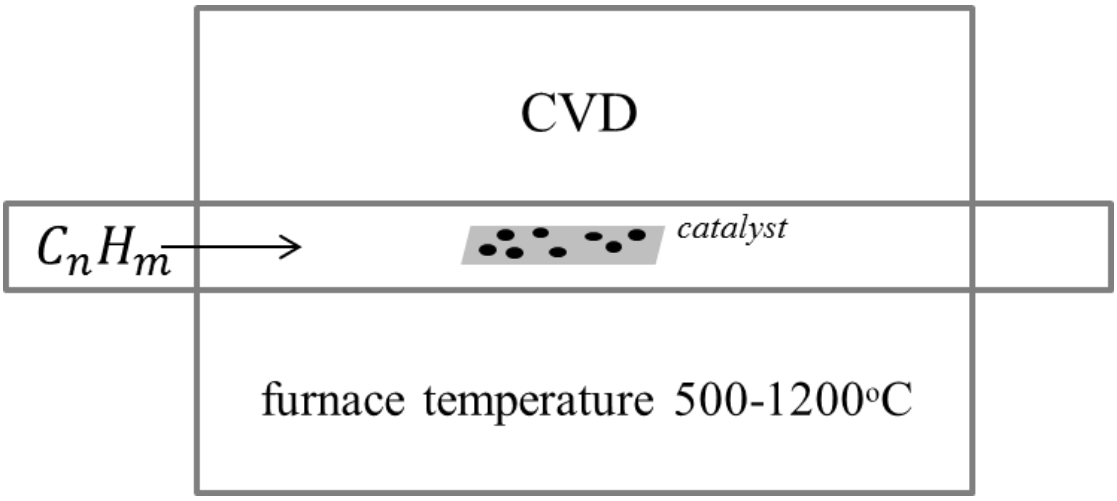

Figure 3-8 Schematics for CVD technique. Hydrocarbons, feedstock of carbon atoms, decompose by catalyst particles at elevated temperatures.

The CVD consists of quartz tube heated in an oven and gas flow system. The gas is flown through the quartz tube including catalyst particles spread over silicon substrate

heated to predetermined temperature. The essential factors of CVD process involve precursors, catalyst particles, and growth temperature. Carbon precursors utilized in CVD are mainly hydrocarbons like methane, ethylene, ethanol, carbon monoxide, acetylene, methanol, benzene, and toluene each possessing particular decomposition temperature for nanotube formations [90, 94]. In the synthesis of SWNT, the rate of carbon precursors is of great importance. The increased temperature can result in high rate of decomposition of hydrocarbon; nonetheless, it can also cause self-pyrolysis of hydrocarbons [90]. Thus, increased concentrations of amorphous carbon lead to deactivation of catalyst process [95]. The favored temperatures for carbon nanotube growth range from $500-1000℃$ [90]. Ideal temperature for growth relies on primarily preferred carbon feedstock and catalyst. The dynamics of the growth is highly dependent on the ambient temperature. Other crucial effect of the temperature is the treatment of readily oxidized catalyst nanoparticles, by bringing back to activated mode [96]. The catalyst nanoparticles used in CVD process mostly are Fe, Co Mo, Ni, Cu, Au, etc. knows as transitional-metal nanoparticles [90]. High carbon solubility and diffusion rates as well as high melting temperatures are essential characteristics to be exploited in the nanotube formations [94]. One the other crucial function of metals is the capability to decompose carbonic molecules during the formation of carbon nanotubes. The catalyst particles can be produced by different fabrication methodologies [90]. For instance, as Moisala et al noted the precipitation of metal salts (nitrates, sulfates and chlorides) and organometallic precursor support are widely used methods[90]. The size distribution of manufactured particle can vary and can be significantly effective in the time of formation. In fact, it has been proposed that the size of catalyst particles may directly be related to the diameter of formed carbon nanotubes [97]. Experimental evidence was conducted by Cheung et al [95], iron particles with average diameter of 3, 9, and 13 nm yielded carbon nanotubes with 3, 7, and 12 nm tubule diameters respectively. The typical range for the diameter size of SWNT is between 0.7 and 4 nm. The smallest size for SWNT is believed to be confined to that of fullerene size (C_{60}) [73].

The exact mechanism for the synthesis of carbon nanotubes is still unclear, nevertheless, the consensus is that at high temperature the hydrocarbons decompose into hydrogen and carbon, carbon atoms dissolve and diffuse into the metal surface and rearrange themselves into a clusters containing hexagons of carbon atoms and finally precipitate to form carbon nanotubes [73, 81]. There are two modes of the carbon nanotube formation. When the catalyst particles are strongly bounded to the support the carbon atom precipitate and begin to grow on top the metal particles which remain bound to surface. It is called root-growth [81]. Conversely, if the metal particles are weakly bounded to the support, the carbon atoms start to precipitate from the bottom of the metal particles suspending them off the surface, called as the tip-growth [81].

The various parameters such as hydrocarbons, catalyst particles, and the formation temperature are essential in CVD process. Their manipulations to enhance the synthesis of particular carbon nanotube is what makes CVD method promising.

In this work, we have used CVD system to growth SWNT. Figure 3-9 depicts growth-setup. It consists of gas tubes of argon and hydrogen, carbon seed bubbler, control unit, and the furnace. The first step of the process is to prepare catalyst nanoparticles, in our case iron chloride. Predetermined amount of iron chloride, concentrations of which affect the SWNT formation, is mixed with photoresist (Shipley 1805). In fact, different molarities of catalyst solutions readily determine the densities of SWNT network. Then the photoresist, doped with Fe_2Cl_3 , is covered on the surface of wafers with a 500 nm thickness. Annealing photoresist in air can cause oxidation of catalyst nanoparticles. This process is necessary to remove organic contaminants from the surface of metal dispersed wafer, in our case silicon oxide. In order to abate iron oxide nanoparticles the substrate is annealed in hydrogen (300 sccm) at 700 ℃ for 20 min. in the quartz tube. Subsequent to the reduction of iron oxide molecules the growth is started by flowing ethanol vapor using carrier flow of Ar (50 sccm) and H_2 (50 sccm) at 920℃. The flow rates of the gases are controlled by control units. After 15 min. we terminate the growth and cool sample to room temperature under Ar (1000 sccm) flow.

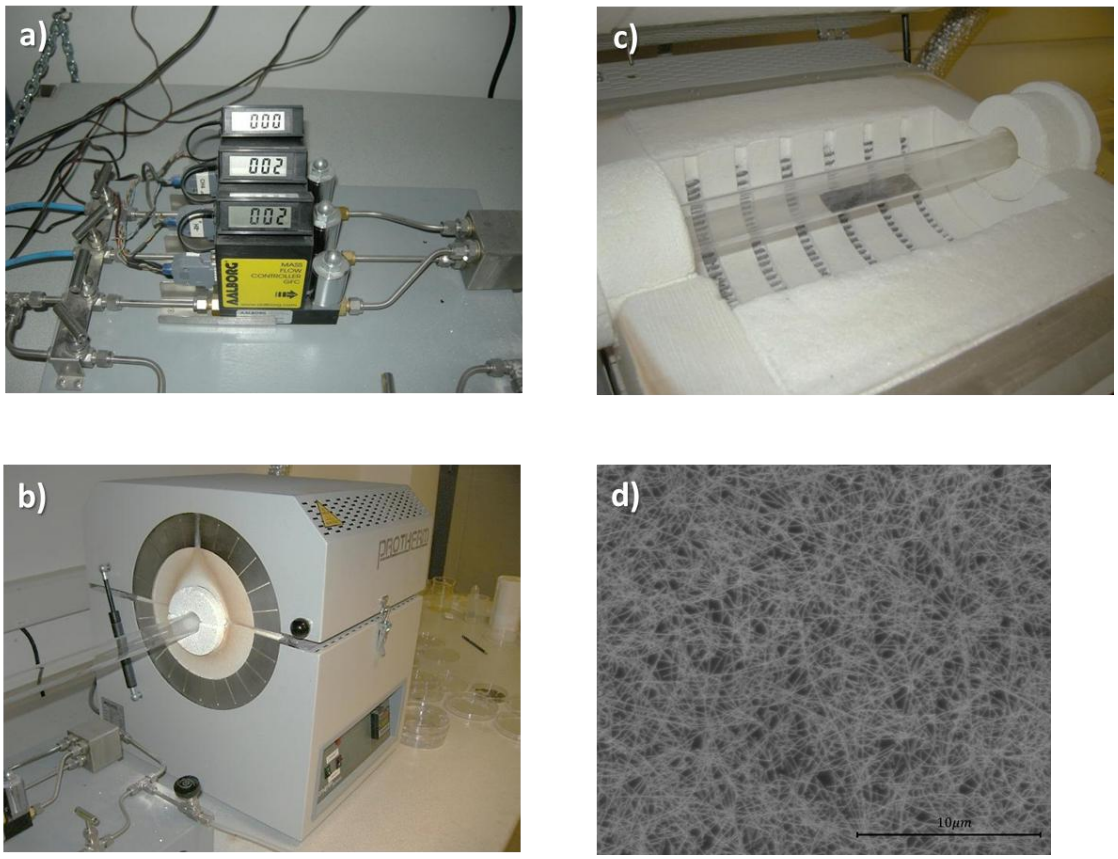

Figure 3-9 CVD system equipment for SWNT growth. CVD system contains (a) furnace with inside quartz silica tube vacuum chamber system, (b) gas flow control units and (c) the sample close-up inside furnace. (d) SEM image of SWNT network.

The characterizations of the samples are done by electron microscope and Raman spectroscopy. The scanning electron microscope (SEM) images (see figure 3-9d) reveal density and uniformity of the SWNT samples grown by CVD. In a similar fashion, the Raman spectra indicate the quality and the number of walls for the carbon nanotubes [98-100]. The peaks at $1317\ cm^{-1}$ (D-band), $1567\ cm^{-1}$ (G-band), and $2657\ cm^{-1}$ (G'-band) are clear indicator of single wall carbon nanotubes (see figure 3-10).

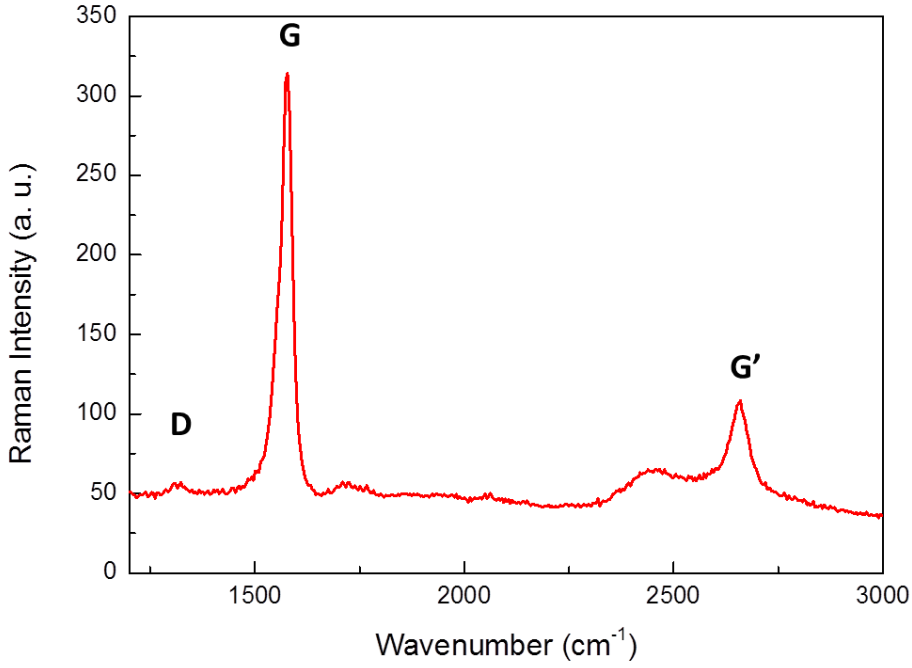

Figure 3-10 Raman spectrum of single wall carbon nanotube. D- and G' bands indicate disorders whiles G-band carries graphitic nature.

The samples grown on Si/SiO_2 substrate can be easily transferred to other surfaces. In our study, SWNT network was transferred to a 50 nm thick gold surface. The property that gold and carbon nanotube strongly stick together than carbon nanotube is held on Si/SiO_2 substrate is base for transferring process. Figure 3-11 depicts the procedure. The SWNT networks were grown by CVD system as described above. We first evaporated 50 nm thick gold film on the SWNT network. Not only the gold layer provides mechanical support for SWNT during the transfer process with low adhesion on SiO_2 surface, but it maintains surface for SPPs. We applied the gold coated surface on a glass slide coated with UV curable polymer. The polymer layer is cured as it exposed to UV light and hence sticks the gold-SWNT layer to the cured polymer surface. The SWNT networks transferred on gold surface after mechanically removing the substrate.

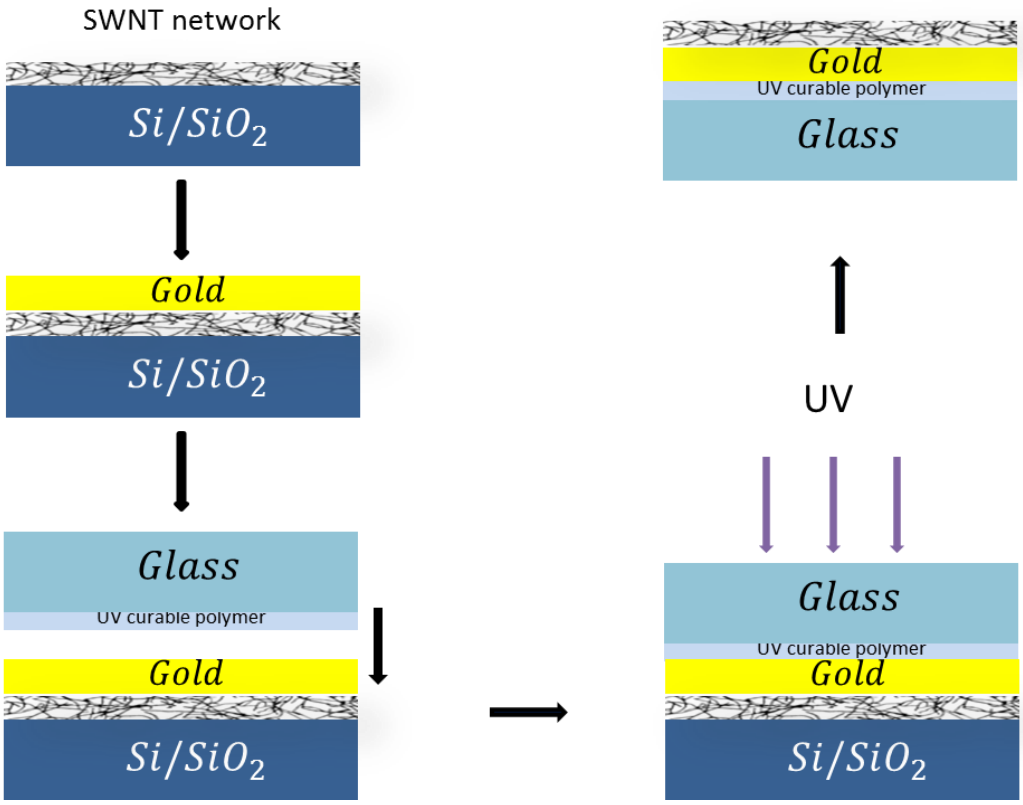

Figure 3-11 SWNT transfer-print process on gold metal surface step diagram.

3.4 Synthesis of graphene

Principal four approaches of the graphene formations are mechanical exfoliation, epitaxial growth on SiC, and CVD method. All those methods have been discussed in this section.

3.4.1 Mechanical exfoliation

Exfoliation method [2, 74] is the first successful method to isolate graphene. As a matter of fact, this method was not the first try of suspending monolayer graphite, earlier work by B. Lang et al have demonstrated formation of mono and multi-layer graphite by decomposing carbon on single crystal Pt substrates [101]. Nonetheless, it was not studied extensively due to the failure to realize graphene's favorable applications at that time.

Graphite consists of large number of carbon stacks bound by van der Waals force. Van der Waals force is relatively weak compared to the covalent bonds, enabling possibility of producing graphene by breaking inter-plane bonds. Exfoliation and cleavage approaches are based on applying mechanical or chemical energy to crack these bonds and separating individual graphene sheets [102]. Basically, exfoliation is the process of peeling. Novoselov et al. [2], have successfully exploited cleavage technique to produce few layers or even single layer graphene. They have used commercial highly oriented graphite sheet and dry etched it by exposing to oxygen plasma to make many deep mesas [2]. The photoresist is used to stick mesas which then removed by scotch tape to peel off the layers. Resultant thin flakes were found to be single to few layer of graphene. Exfoliated graphene can be as large as 100μm and are easily transferred to different substrates.

3.4.2 Thermal decomposition of SiC

One of the first growths of graphitic structures by silicon (Si) sublimation from Silicon Carbide (SiC) substrates was demonstrated in 1975 [103]. Electronic properties of those materials were found to be similar to that of isolated graphene [104]. The process includes thermal decomposition of Si on the surface plane (0001) of 4H- and 6H-SiC wafer [102]. The formations of graphene sheets caused when SiC wafer is heated to 1500℃ leading to sublimation of Si atom leaving carbon atoms which then rearrange themselves into graphene sheets [104]. Such epitaxially grown graphene were found to have single to few layers [102]. Compatibility of SiC formation of graphene with standard semiconductor device fabrication technology and capability of large scale production have attracted attention of semiconductor industries and considered to be viable technique [104]. A comprehensive review concerning such issue was reported by J. Hass et al. [105].

3.4.3 Chemical vapor deposition synthesis of graphene

Growing graphene by chemical vapor deposition is considered as the most promising technique. Its cost, controllability, grain size, etchability and transferability of grown graphene, and large scale area production are widely accepted in semiconductor industries [106]. CVD method is capable of producing centimeter sized continuous

graphitic sheets. The process involves epitaxial growth of single to few layer graphene by flowing mixture of methane and hydrogen gases at an elevated temperatures catalyzed by metals such as Ni, Cu, Co, Pt, and Ir [107]. Methane and Ethanol are widely used carbon feedstock molecules. Similar to carbon nanotube growth metal catalysts effectively function the patterned growth of graphene at particular locations with desired geometries [107]. Catalyst films are responsible for decomposition of carbon precursor molecules on the surface or within the catalyst itself additionally providing support graphene during growth process. Copper and nickel are widely used substrate materials owing to its cost, grain size, and etchability [94]. Carbon segregation[108] or precipitation[109] is proposed as a process mechanism in CVD growth of graphene on Ni catalyst substrate Li et al.[94]. Authors note the significance of the difference in concepts between segregation and precipitation. That's, according to them, segregation referred to compositional heterogeneity in thermal equilibrium under conditions which correspond to a "one phase" field, while precipitation was caused by inhomogeneities subsequent to equilibrium "phase separation". Also Li at el. [94] mentioned spacious variations in thickness from single to multiple layers on metal surface were discovered on graphene samples grown on Ni foils. The inhomogeneity was caused by high solubility of carbon atom in nickel. It is claimed that graphene mono-layer starts to grow by carbon segregation then precipitation induces further top layer formations [110]. In order to terminate multiple layer growth fast cooling of samples is necessary. Unlike nickel, copper does not have over saturation due to its low solubility of carbon atoms in Cu [94]. Additionally, very large grain sizes can be obtained by annealing copper. This makes copper a viable thin film catalyst candidate in graphene synthesis. Previous studies showed that graphene films grown on the surface catalyzed by Cu exhibited predominantly mono-layer with less than %5 two- and three-layer graphene flakes, and these flakes would not grow larger for with time [111]. Furthermore, Li at el. have demonstrated that it takes less than 3 min. to grow single layer graphene, and that the growth is self-limiting due to the lack of catalyst to promote the growth and thus metals with low carbon solubility provide possibilities for large-scale growth of graphene.

In our experiments, graphene layers were synthesized on copper foils by chemical vapor deposition (refer to figure 3-12). The copper foils were placed in a quartz chamber and heated to 1050 ^{o}C under flow of hydrogen and argon gases. In order to reduce the oxide layer, the samples were annealed for 30 min at 1050 ^{o}C. After the annealing process, methane gas with a rate of flow of 7 sccm was sent to the chamber for 10 min. The chamber pressure was kept at 5 Torr during the growth. The growth was terminated by stopping the flow of methane gas and the chamber was cooled back to the room temperature. Figure 3-12 shows chemical vapor deposition set-up for graphene. The grown graphene can be characterized using Raman spectroscopy. Typical signal for monolayer graphene is shown in figure 3-13a where the peak at $1576\,cm^{-1}$ is G-band and the peak at $2670\,cm^{-1}$ is 2D band. These bands demonstrate the distinctions of graphene layer from that of bulk graphite [99]. In addition, the D-band at $\sim 1350\,cm^{-1}$ represents defect mode. Since, D-band peak is low the graphene samples indicate high quality. Figure 3-13b shows the Raman spectra comparison for mono-, bi- and trilayer graphene. As can be seen, there are no significant distinctions between single and few layers of graphene, and hence behave alike. Figure 3-13c demonstrates the graphene on copper and transferred graphene. In figure 3-13d, the transmission spectra of graphene on quartz substrate is depicted. %2 of absorbance is observed for each layer of graphene.

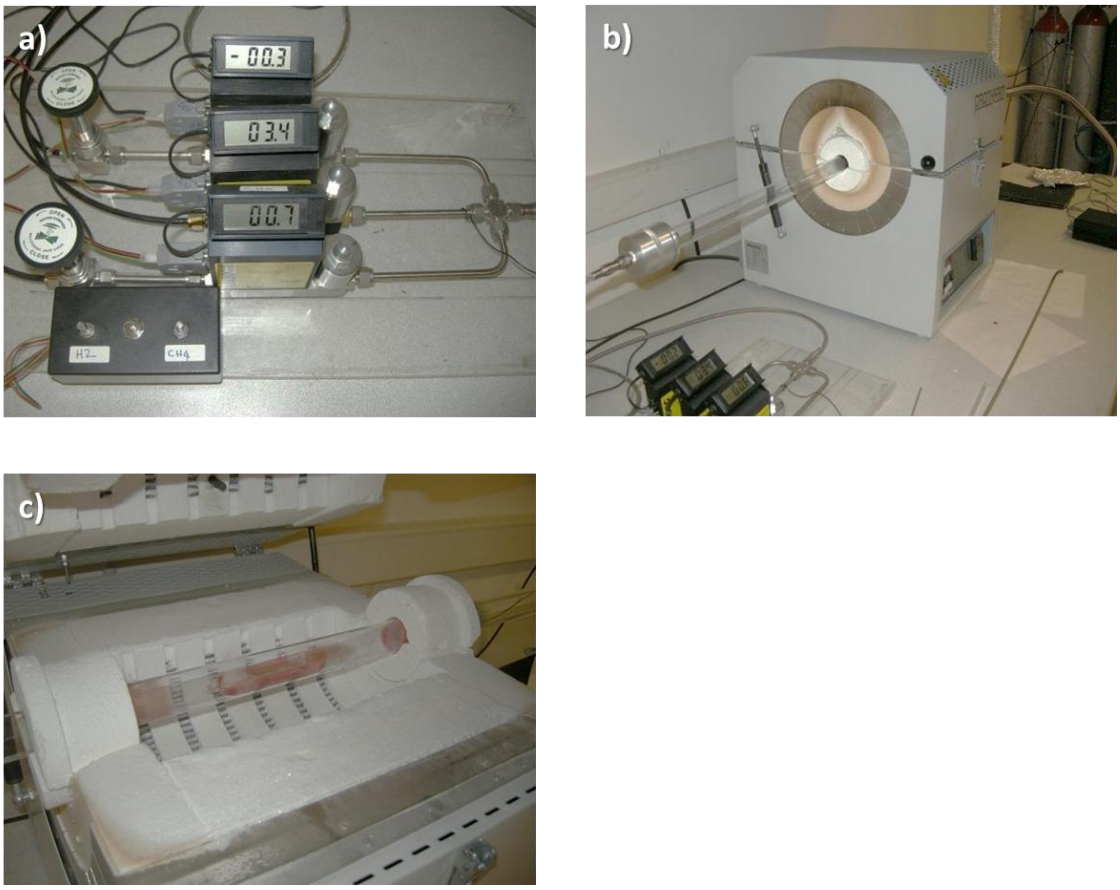

Figure 3-12 CVD system equipment for graphene growth. CVD equipment includes (a) gas flow control units, (b) sample close-up inside furnace, (c) furnace and inside quartz silica tube integrated with vacuum chamber system.

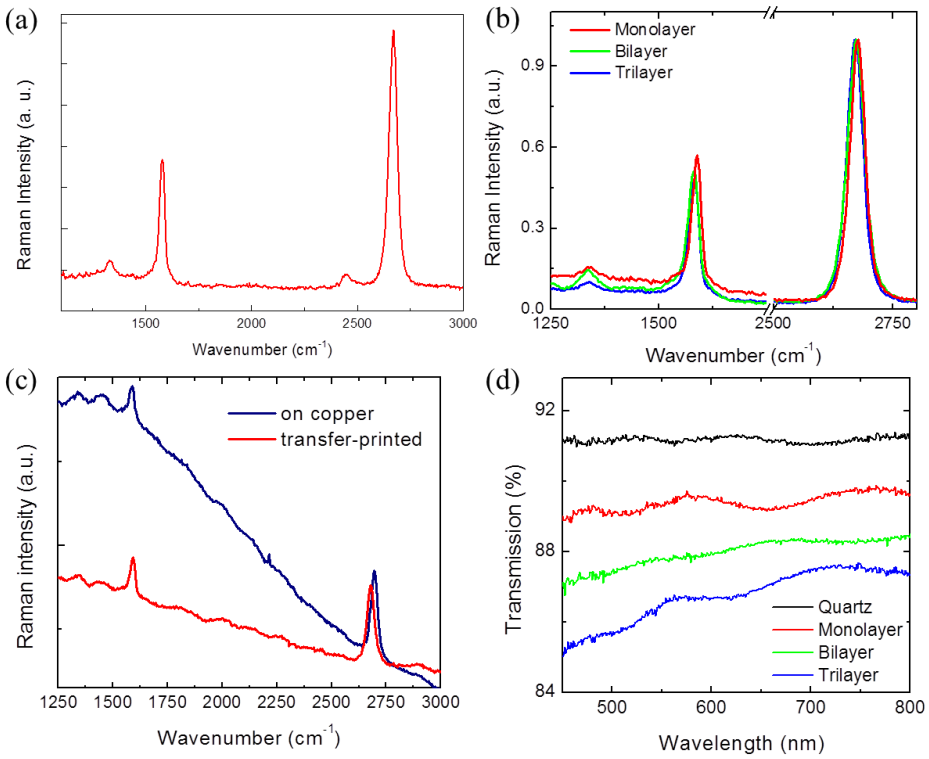

Figure 3-13 Raman and transmission spectra of graphene layers grown on Cu foil. (a) Raman spectrum of single layer graphene. (b) Raman spectra of mono-, bi-, and trilayers of graphene and (c) graphene on copper and transferred graphene. (d) Absorption spectra of number of graphene on quartz substrate.

Graphene grown on Cu foil by CVD method (figure 3-12) is easily transferrable. In this work we have been able to repeatedly transfer graphene films on the surface of quartz crystal microbalance. Figure 3-14 schematically demonstrates the transfer-print process. The graphene coated copper foils were spin coated with a photoresist (PR, AZ5214) with a thickness of 1.4 µm. A flat elastomeric stamp (PDMS) was placed on the PR layer and the copper foil was etched by 1 M iron chloride solution. After the etching, the PR with graphene layer remains on the PDMS stamp. The stamp was applied on gold coated quartz crystal microbalance and heated to 100 ^{o}C to release the PR. After removing the stamp, the PR was removed in acetone. After the transfer process, we have large area graphene on gold surface. In order to get multilayer graphene on the gold surface, we performed multiple transfer process.

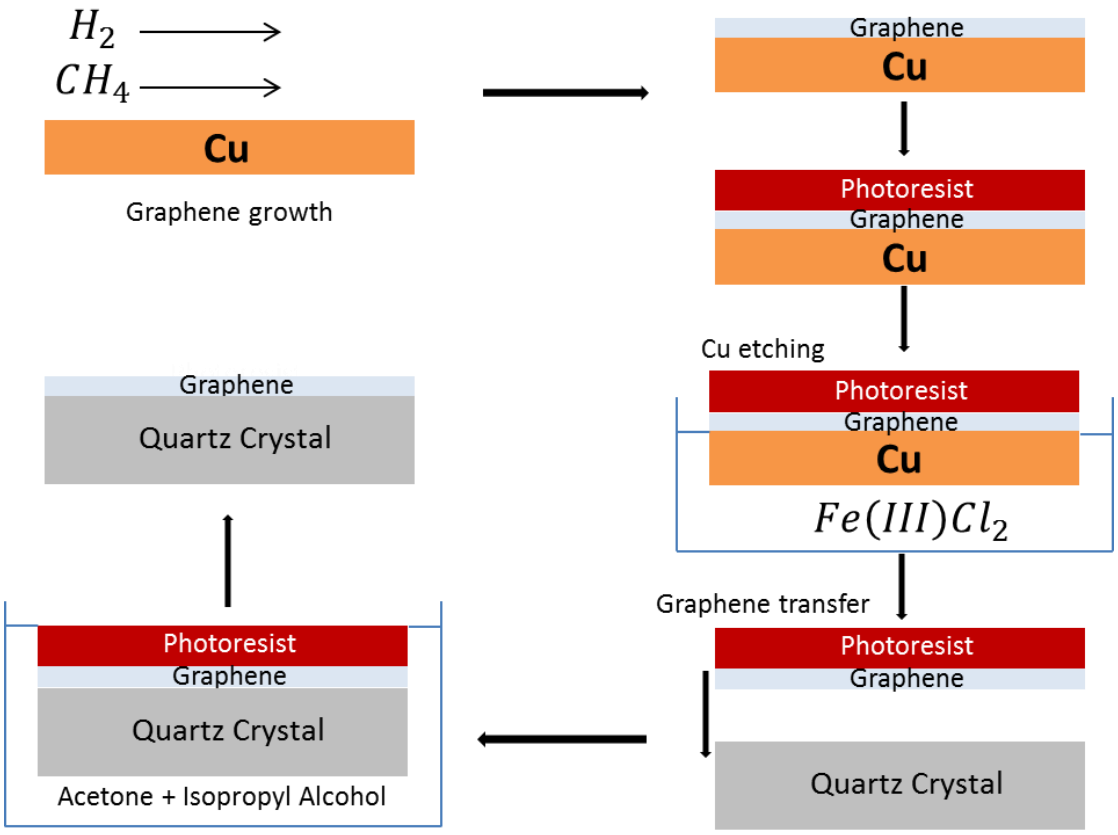

Figure 3-14 Schematics for transfer-print procedure of graphene sheet on quartz crystal surface.

Chapter 4

Probing Molecular Interactions on Carbon Nanotube Surfaces

This chapter presents a method for probing molecular interaction on single-walled nanotube surfaces using surface plasmon sensor. SWNT networks were synthesized by chemical vapor deposition and transfer-printed on gold surfaces. We studied the excitation of surface plasmon-polaritons on nanotube coated gold surfaces with sub-monolayer, monolayer, and multilayer surface coverage. Integrating the fabricated sensor with a microfluidic device, we were able to obtain binding dynamics of a bovine serum albumin (BSA) protein on SWNT networks with various tube densities. The results reveal the kinetic parameters for nonspecific binding of BSA on SWNT surface for various tube densities. Some part of this chapter is submitted for publication in *Applied Physics Letter* as "Probing Molecular Interactions on Carbon Nanotube Surfaces using Surface Plasmon Resonance Sensors".

4.1 Surface plasmon polariton

SPR sensors rely on surface plasmon polaritons (SPPs) excitations. Environmental changes affect the effective refractive index of the medium and thus alter resonance conditions. These changes are reflected on the shifts either in resonance angle or wavelength producing detectable signals. Surface plasmon polaritons are principally two dimensional electromagnetic waves propagating at the interface between a dielectric and a conductor [112]. These waves are caused by the couplings of the

incident beam's photons with the electron gas of the conductor. In order for the coupling to occur certain conditions must be satisfied, that's the energy and the momentum must be conserved [113]. To understand it better we have to analyze the dispersion relations of the surface waves in the medium with respect to the angular frequency (ω) and wavevector (k). Since the propagation constant of the surface plasmons (SPs) β is greater than the wavevector of the light beam k, the SPP cannot be excited by direct light [112]. In other words, the projection of the wavevector of the beam, incident at an angle θ, along the interface is $k_x = ksin\theta < \beta$ prevents the phase-matching. As can be seen in the figure SPP dispersion curve lies outside of the light cone. Nevertheless, the matching can be possible by employing high index prism in front of the metal. By that way wavevector along the surface will suffice to excite SPPs, $k_x = n_p ksin\theta$ where n_p is refractive index of the prism (see figure 4-1).

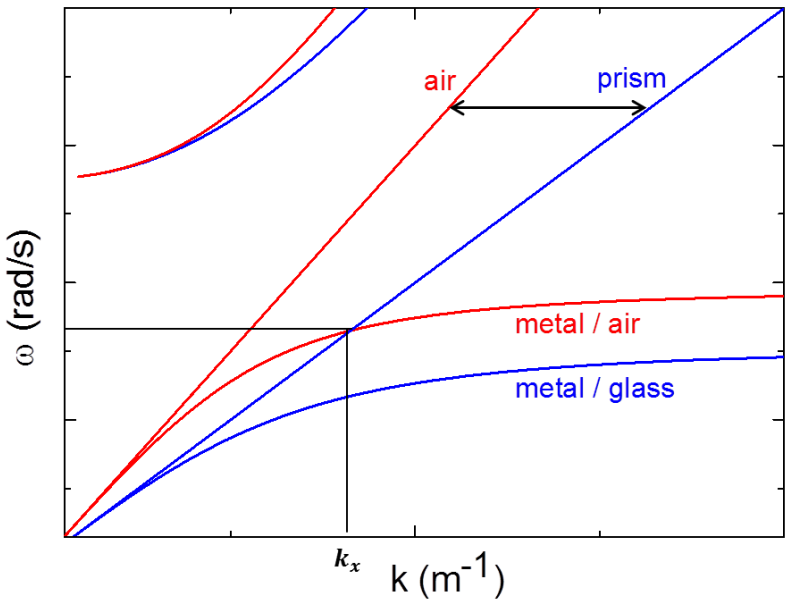

Figure 4-1 Dispersion curve of surface plasmon polaritons at at metal/air and metal/glass interfaces. Light line in prism is tilted enabling momentum energy match for SPP excitations. The plasmons at the metal/glass interface cannot be excited since the dispersion curve is out of light cone.

The dispersion relation (see figure 4-1) is given by,

$$\beta = \frac{\omega}{c}\sqrt{\frac{\varepsilon_d \varepsilon_m}{\varepsilon_d + \varepsilon_m}} \tag{4.1}$$

where c is the speed of light, $\varepsilon_d \; and \; \varepsilon_m$ are the dielectric constants of dielectric and metal respectively. The dispersion curve was plotted for air ($\varepsilon = 1$) and assuming the Drude model for electron gas [113]. There are two distinct configurations which include prism coupler, Kretschmann and Otto, see figure 4-2 [114]. The former one is most commonly used configuration due to its practicality. It includes thin metal film evaporated on one surface of high index prism. The photons of the beam falling onto the interface at angle greater than the critical angle penetrate through the metal and couple with the surface plasmons. Unlike Kretschmann configuration, the Otto geometry includes air gap between the prism and metal film. In this configuration, the beam is totally internally reflected at the prism-air interface creating propagating evanescent waves which excite surface plasmons at the air-metal interface.

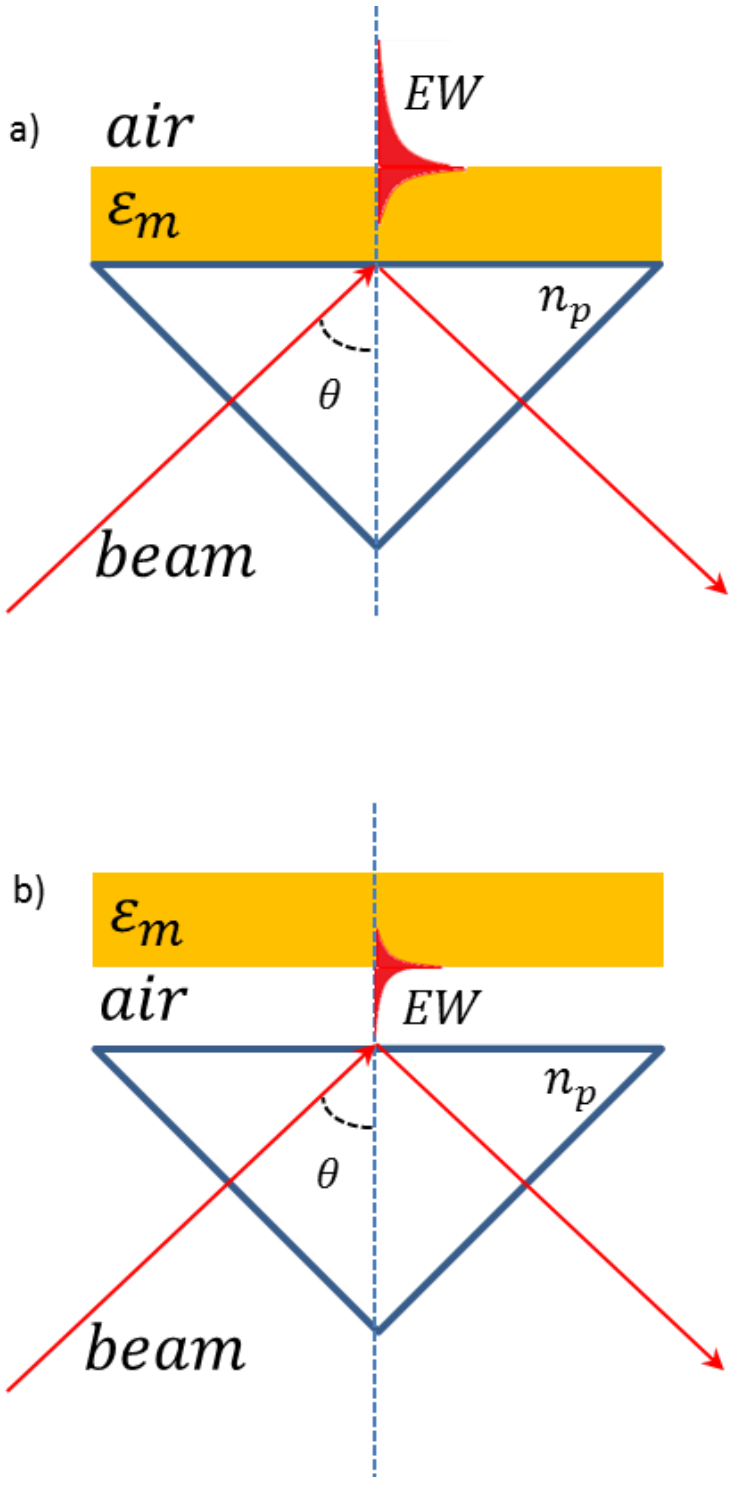

Figure 4-2 Surface plasmon polariton excitation geometries. a) Kretschmann configuration b) Otto configuration.

4.2 Probing Molecular Interactions on SWNT

In this work we integrated surface plasmon resonance (SPR) sensors with networks of single-walled carbon nanotubes to study interactions between SWNT and organic molecules. SPR sensors provide surface specific detection schemes with superior sensitivity. The evanescent field of surface plasmons (SPs) decays exponentially from the surface with a decay length of a few hundreds of nanometers. Surface specific detection together with the high sensitivity allows the widespread acceptance of SPR sensors. Here we implement SPR sensors to probe dynamics of a medium size protein on SWNT surfaces. SWNT networks with various tube densities were grown by chemical vapor deposition and then transfer-printed on gold surfaces. To understand the effects of SWNT on plasmonic properties of the surface, we first measured the resonance characteristics of SPPs on SWNT functionalized gold surface. As a demonstration we studied binding dynamics of bovine serum albumin protein on SWNT network with various tube densities. The sample preparation is demonstrated in figure 4-3.

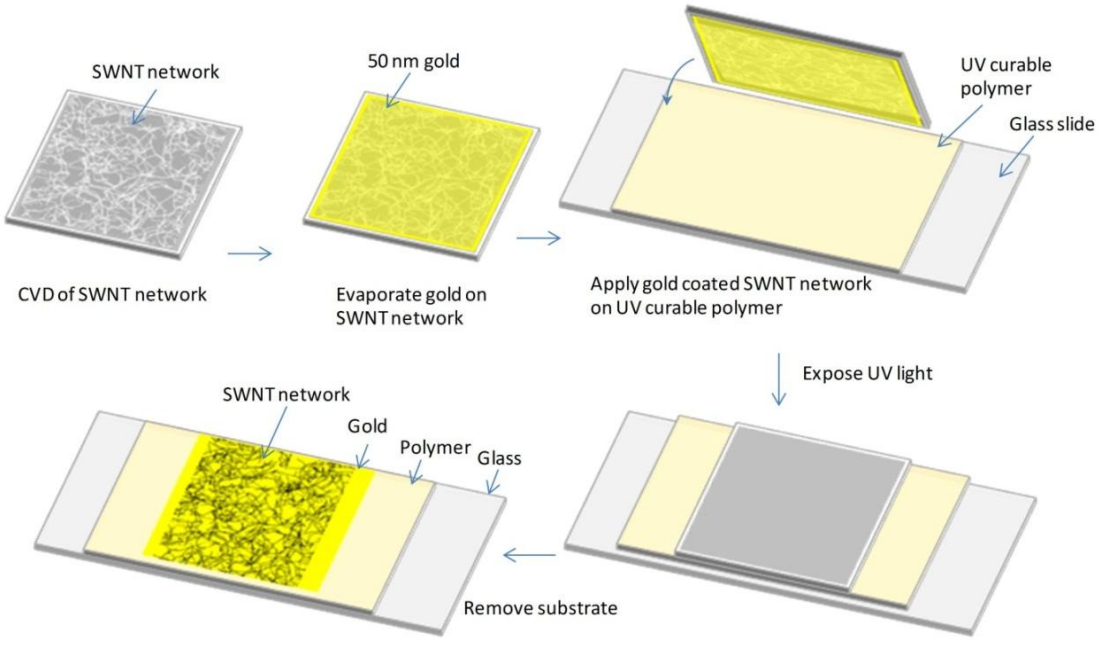

Figure 4-3 Transfer printing process of SWNT network grown on SiO_2 coated Si substrates.

The SWNT networks were grown by catalytic chemical vapor deposition technique using iron nanoparticles as seeds for the growth. The process starts with coating the wafers with a 500 nm thick photoresist (Shipley 1805) doped with Fe_2Cl_3 having concentration of 1-3 mM. Annealing the photoresist in air results in dispersed iron oxide nanoparticles on the SiO_2 surface. Iron oxide particles are reduced by hydrogen (300 sccm) as the temperature of the samples reaches to 920 ^oC. After reducing the iron oxide particles, we started the SWNT growth by flowing ethanol vapor in to the chamber using a carrier flow of 50 sccm Ar and 50 sccm H_2 at 920 ^oC. After 15 minutes, we terminated the growth and cooled the samples back to the room temperature under a flow of Ar. The density of SWNT networks was controlled by changing the concentration of Fe_2Cl_3 in the photoresist layer. Following the growth, we transferred SWNTs on metal substrates. Growing SWNT directly on 50 nm gold surface is not possible because of dewetting of gold layer on SiO_2 surface[115]. In order to solve this problem, we developed a transfer printing process. Fig. 1 shows the steps of the transfer-printing process of SWNT networks to the gold surface. We first evaporated 50 nm thick gold film on the SWNT network. The role of the gold layer is twofold; first it provides mechanical support for SWNT during the transfer process with low adhesion on SiO_2 surface, second, it supports surface plasmon-polaritons. We applied the gold coated surface on a glass slide coated with UV curable polymer (Epo-Tek, OG146). A 5-minute exposure of UV light cures the polymer layer and sticks the gold-SWNT layer to the cured polymer surface. The SWNT networks on gold surface are achieved by mechanically removing the substrate with a razorblade.

Figure 4-4 shows the scanning electron micrographs of SWNT networks with various tube densities on SiO_2 substrates. The tube density was controlled by changing the catalyst concentration. The surface coverage of the SWNT networks ranges from submonolayer (~5% coverage) to multilayer. We named the three representative tube density as D1 (submonolayer), D2 (monolayer) and D3 (multilayer). The tube densities for D1, D2 and D3 are ~1 SWNT/μm^2 ~10 SWNT/μm^2 and ~50 SWNT/μm^2, respectively. The carbon nanotubes are primarily single-walled with tube diameters from 0.7 nm to 4 nm.

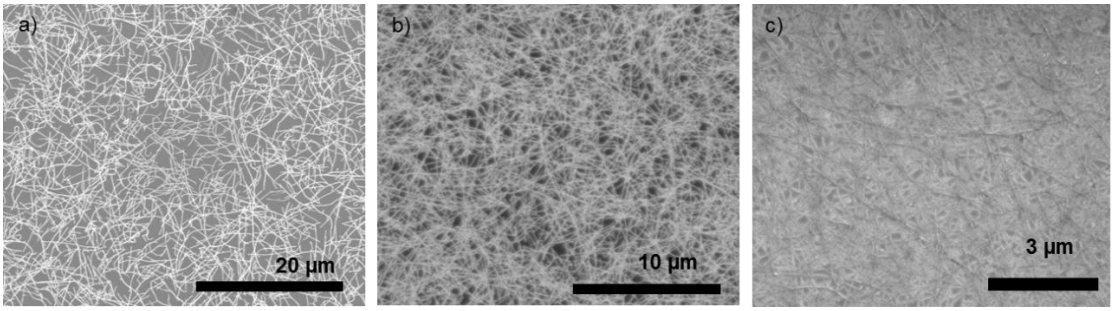

Figure 4-4 Electron micrographs of SWNT networks with various tube densities grown by chemical vapor deposition on SiO_2 substrates. Tube density was controlled by changing the concentration of the catalyst. These networks are named as sub-monolayer (D1=1 SWNT/µm^2), monolayer (D2=10 SWNT/µm^2) and multilayer (D3=50 SWNT/µm^2), respectively. The tube diameter ranges between 0.7 nm to 4 nm.

Before studying the binding kinetics, we first characterized the plasmonic properties of the gold surface coated with SWNT network. Figure 4-5 shows the experimental setup used to excite SPPs. Due to the confined nature of SPPs, their momentum is larger than the momentum of light in free space. The momentum mismatch can be compensated using a prism with high index of refraction. This arrangement is known as Kretschmann configuration. A supercontinium laser attached with an acousto-optical modulator (Koheras Inc., SuperK versa) was used as a tunable light source with a spectral width of ~1nm. Surface plasmon-polaritons are excited by TM polarized light at the resonance angle where the phase matching condition is satisfied as

$$\sin(\theta_c) = \frac{k_{spp}}{n_p k_0} = \frac{1}{n_p}\sqrt{\frac{\varepsilon_m \varepsilon_d}{\varepsilon_m + \varepsilon_d}} \qquad (4.2)$$

where k_{spp} is the momentum of surface plasmon-polaritons, n_p is the refractive index of the prism, k_0 is the momentum of light in free space, ε_m and ε_d are the dielectric constant of the metal and the medium, respectively. The refractive index of the prism is ~1.52. The 50 nm thick gold layer used during the transfer printing process supports the SPPs. In order to obtain the dispersion curves, we measured the polarization dependent reflectivity of the surface as a function of wavelength (from 400nm to 1000nm) and incidence angle (from 40 deg. to 48 deg.) with a precision of less than 1nm and 0.01 degrees, respectively.

Figure 4-6 shows the reflectivity maps from the SWNT coated gold surfaces as a function of excitation wavelength and incidence angle. The wavelength scans the energy of the exited SPPs and the angle defines the momentum. The maps were obtained from the TM polarized reflection spectra. When the resonance condition (eqn. 4.2) is satisfied, the reflectivity goes to a minimum value. The resonance wavelength is obtained from the minimum value. We observed that as the surface coverage increases, the resonance wavelength red-shifts and the spectral width of the surface plasmon resonance gets broader, which is likely because of additional optical losses (scattering losses) associated with the high density of SWNT networks.

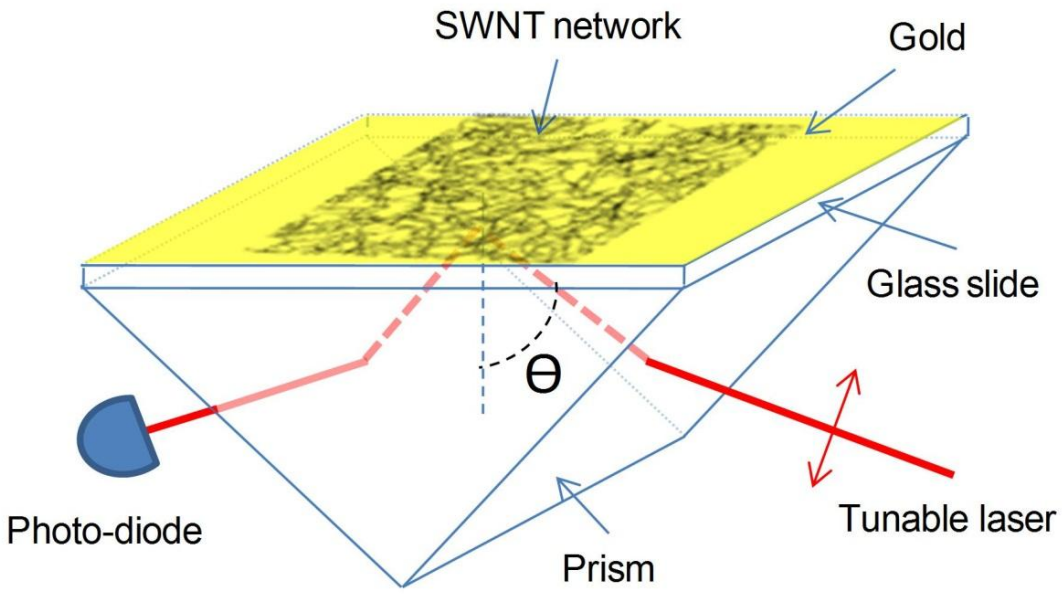

Figure 4-5 Experimental setup (Kretschmann configuration) used to excite SPP on metal surface coated with SWNT network. The thickness of the gold layer is 50 nm. The prism is mounted on a double rotary state. The reflected beam is detected by a photodiode. The incidence angle and the wavelength of the laser are controlled with a precision of less than 0.01 deg. and 1 nm, respectively.

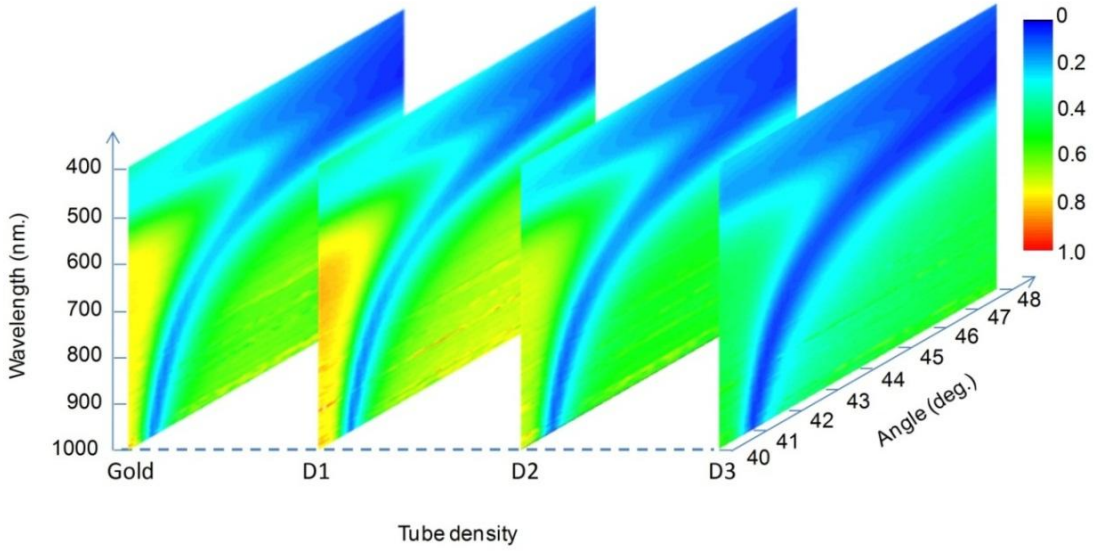

Figure 4-6 The reflectivity maps (angular dispersion curves) from the SWNT coated gold surface as a function of incidence angle and the excitation wavelength. The light source is TM polarized. As the density of SWNTs network increases, the effective index of the surface plasmon-polaritons increases resulting in a red shift in the plasmon resonance wavelength. The color map shows the scale for the reflectivity.

The characteristic surface plasmon absorption dip can be seen not only by scanning the wavelength of the excitation, but also it can be obtained by scanning the incidence angle with monochromatic excitation. Figure 4-7 summarizes the change in the reflection spectra with increasing tube density. Figure 4-7a shows the reflection spectra of the surface recorded at an incidence angle of 44 deg. There are two resonances; the one that is at around 470 nm is due to the bulk plasmon absorption, the second resonance at around 605 nm is due to the surface plasmon-polaritons. The bulk plasmon absorption is independent of the surface coverage. Angular dependence of the reflectivity from the surfaces is shown in figure 4-7b. The resonance angle increases with increasing tube density. Figure 4-7c and 4-7d show the change of resonance wavelength and resonance angle as a function of tube density, respectively.

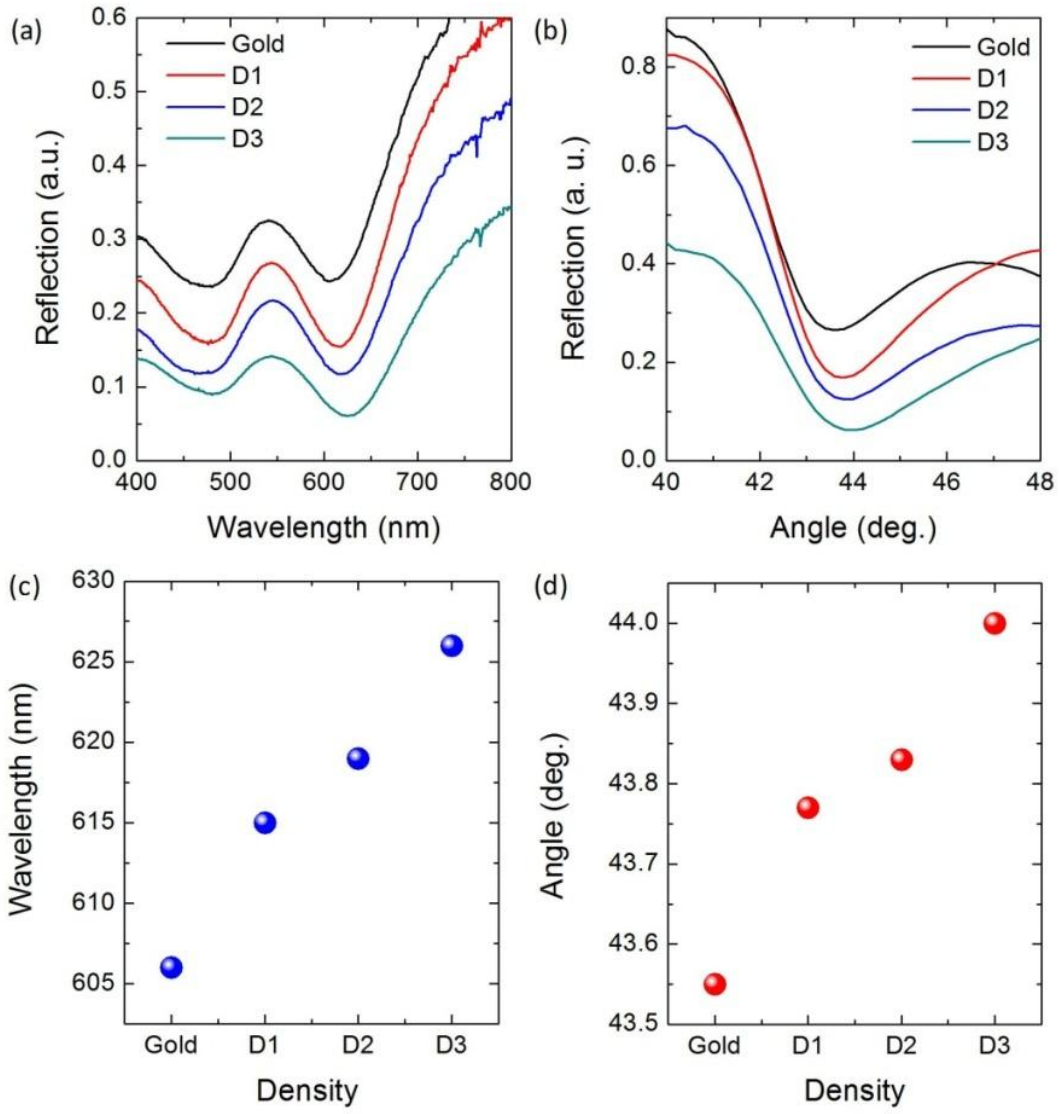

Figure 4-7 (a) Reflection spectra from the gold surface for various tube densities. The incidence angle is 44 deg. There are two resonances in the reflectivity spectra; bulk plasmon resonance of around 450 nm and surface plasmon resonance of around 600 nm. (b) Reflectivity of the surface as a function of incidence angle for various surface coverage. (c,d) Dependence of surface plasmon resonance wavelength and angle on the surface coverage of SWNT networks, respectively.

The gold surface functionalized with SWNT network provides us a unique platform to probe binding interaction between SWNT surface and organic molecules. As a proof of principle, we studied nonspecific binding of a bovine serum albumin (BSA) protein on SWNT surface In order to probe binding interactions of proteins on SWNT network, we integrated the SPR sensor with a microfluidic device. Figure 4-8a shows the fabrication steps the device. The device consists of an elastomeric flow chamber sealed on the SWNT functionalize gold surface. For efficient coupling of SPP, the thickness of the gold layer is chosen to be 50 nm. A TM polarized diode laser (λ=635 nm) and a prism with a high index of refraction (BK7, n_p=1.78) are used to excite SPPs. The reflectivity as a function of incidence angle is given in Figure 4-8b. The SPR angle is at 57 deg. After setting the incidence angle to the resonance angle, we first run DI water through the flow chamber for 5 min. When the SPR signal was stabilized, we started the flow of 100 nM BSA solution and recorded the SPR signal for 30 minutes. We repeated the same procedure for a bare gold surface and gold surfaces coated with three different SWNT networks shown in figure 4-4. The time traces of SPR signal for binding interaction of BSA on the various surfaces are shown in figure 4-8c. After the SPR signal saturated, we washed the surface with DI water. We did not observe any change in SPR signal, which indicates that BSA is kinetically stable on SWNT surface.

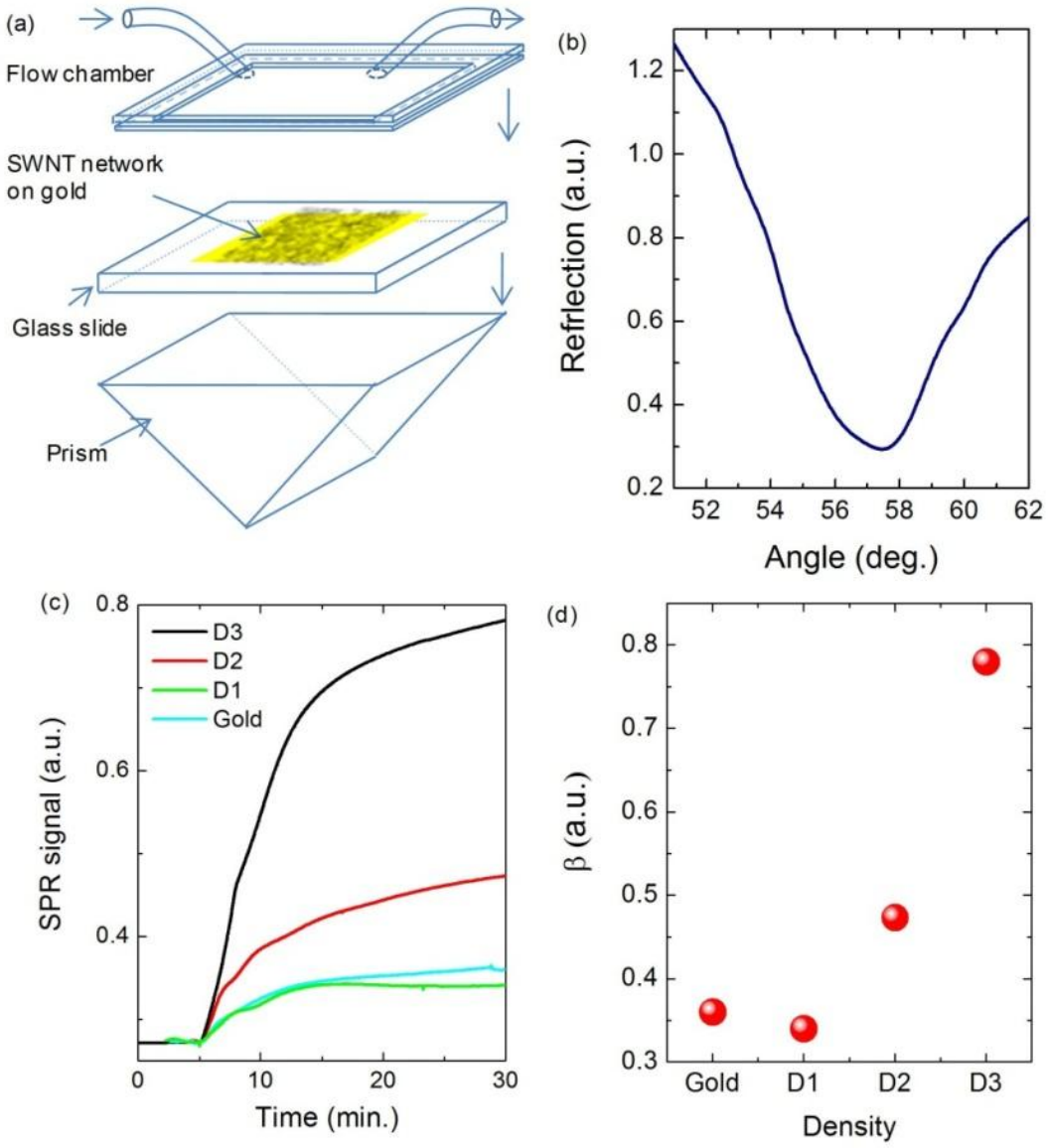

Figure 4-8 (a) Schematic representation of the microfluidic device integrated with SPR sensor functionalized with SWNT network. The flow chamber is sealed on SWNT coated gold surface. The glass slide is attached on the prism using an index matching fluid. (b) Reflectivity of the gold surface as a function of incidence angle at 635 nm. The resonance angle is 57 deg. (c) Time trace of SPR signal for binding interaction of BSA on gold surface coated with various SWNT network. The concentration of BSA is 100 nm. (d) The extracted parameter (β) quantifies the available binding sites on the surface of SPR sensor. The β-parameter for gold and submonolayer SWNT networks is around 0.35. As the density of SWNT increases the β-parameter changes from 0.35 to 0.8 while the association constant stays constant with a value of 0.56×10^5 M^{-1} sec^{-1}.

To understand the nonspecific binding of BSA on SWNT network, we used a first-order pseudo-kinetic equation. Since we employed a flow cell the number of molecules in the medium is much higher than the available binding sides on the surface. The pseudo-kinetic equation can be written as

$$\frac{dA}{dt} = k_a C(\beta - A) - k_d A \tag{4.3}$$

where A is the concentration of molecules binding to the surface, k_a is the association rate constant, β is the concentration of free binding sides, and k_d is the dissociation rate constant. Since we did not observe any disassociation from the surface the value of k_d is zero. With these conditions, the solution of the kinetic equation is

$$C(t) = \beta(1 - e^{-k_a A t}) \tag{4.4}$$

In the linear regime of the reflection spectrum, the SPR signal is proportional with the concentration of molecules binding to the surface. We obtained β and k_a values from the least squares fitting of the time trace of SPR signal for various SWNT networks. Figure 4-8d shows that the extracted values of β which quantifies the concentration of free binding sides. The concentration of free binding sides increases with the tube density while the association constant stays constant with a value of 0.56×10^5 M^{-1} sec^{-1}.

As a conclusion, we present a SPR sensor to probe binding dynamics of organic molecules on SWNT surfaces. SWNT networks with various tube densities were grown by chemical vapor deposition and then transfer-printed on gold surfaces. We characterized the plasmonic properties of SWNT coated gold surfaces. As a demonstration we studied binding dynamics of bovine serum albumin protein on SWNT networks with various tube densities. We observed that the concentration of free binding sides increases with the tube density while the association constant stays constant with a value of 0.56×10^5 M^{-1} sec^{-1}. We anticipate that SWNT functionalized SPR sensors could provide a sensitive means for probing adsorption of organic molecules on surfaces of SWNT.

Chapter 5

Probing Interfacial Processes on Graphene

This chapter presents a method for probing interfacial processes on graphene surface using mass detection. Graphene layers were synthesized by chemical vapor deposition on copper foils and transfer-printed on a quartz crystal microbalance (QCM). Probing the mechanical resonance of the QCM, we were able to measure mass density of single layer graphene. We extended the developed technique to probe binding dynamics of proteins on graphene surface. Furthermore, we monitored oxidation of graphene surface under oxygen plasma by tracing the changes of interfacial mass of the graphene layer.

5.1 Interfacial mass detection with piezoelectric transducers

Ward and Buttry in their paper [116] reviewed basic properties, practical methods and applications of mass-sensing piezoelectric crystal sensors. As discussed, a principle phenomenon behind the mass-sensing transducers is converse piezoelectric effect, which is basically the induced stress on piezoelectric material by applied electric field. In fact, if AC voltage is applied across piezoelectric crystal, it causes an alternating strain field which in turn creates acoustic standing waves in quartz crystals. These crystals prefer to oscillate at resonance frequency with high quality factor Q, which make them ideal oscillators [117]. Here the symmetry of the crystal plays crucial role in electromechanical stresses enabling various modes of couplings. Such modes are

consequent for diverse class of acoustic waves, propagations, and particle displacements. For instance, electric field across AT-cut quartz causes shear vibrations, see figure. Furthermore, thickness shear mode specified by AT-cut crystal is used to describe mass-sensing. The shear motion is bound by two electrodes and analogous to standing wave with length L. Hence the fundamental frequency of the string is equal to $\left(\frac{S}{m_l}\right)^{\frac{1}{2}}/2L$ where S is the tension on the string, m_l is the mass per unit length, and L is the length of the string, and dependent on the mass. Similarly, AT-cut quartz possesses fundamental frequency as $f_0 = \left(\frac{\mu}{\rho}\right)^{\frac{1}{2}}/2t_q$ where t_q is the thickness, μ is the shear modulus and ρ is the density of the quartz crystal. An increase in the thickness of quartz crystal results in the decrease of fundamental frequency. Sauerbrey demonstrated the mass-frequency dependence in terms of foreign layer depositions on thickness shear mode quartz crystal. The assumption lies in that the deposited foreign mass becomes an extension of the quartz crystal, and hence frequency change can be expressed as:

$$\Delta f/f_0 = -\Delta t/t_q \tag{5.1}$$

The linear relationship of the frequency shift and the variation of mass are summarized in Sauerbrey's equation.

$$\Delta f = -\frac{2n{f_0}^2}{\sqrt{\rho_q \mu_q}}\Delta m \tag{5.2}$$

where f_0 is the resonant frequency of the fundamental mode of the quartz crystal. For AT cut, 5MHz quartz crystal, the mass density is ρ_q=2.648 g cm^{-3} and the shear modulus is μ_q=2.947x10^{11}g cm^{-1}s^{-2}. The assumption behind Sauerbrey's equation is that the mass distribution is uniform and cover entire electrode region of the quartz. It is significant due to the variations in the sensitivities as the shear mode amplitude drops away from the center to the edges [118]. The liquid contact mode is clear in quartz crystal microbalance devices as the particles move parallel to the surface. Although, the

density and viscosity of the liquid do affect the operating frequency of the quartz crystal, the mass sensitivity stays unaffected in the environment of the liquid. Ward and Buttry also claimed that one disadvantage is the QCM approach cannot distinguish changes caused by either mass depositions or viscoelasticity of thin films or liquids. Nevertheless, this can be overcome using impedance or network analyzer and measuring Q factor which defines width of resonance curve and energy dissipated during oscillations. Since Q is inversely proportional to any viscous effect, the measurement reveals changes in mass. Moreover, QCM transducers are able to track the real time kinetic processes in the media. The primary factor of the resolution is the time that takes to reach equilibrium between mass deposits and device. This limit relies on the Q and given by $Q/\pi f_0$ [119]. For example, the AT-cut quartz has Q values as high as $10^4 to\ 10^6$ for vapor and nonviscous loads and responds rapidly while for liquids Q value is low ($\sim 10^3$) hence time resolution is around milliseconds. Nonetheless, even such resolutions are sufficient to time-trace the kinetic processes, nucleation, growth, and dissolution [120].

5.2 Integration of graphene with QCM

To integrate graphene with QCM, we developed a transfer-printing process. We used AT-cut, α-quartz crystal (331μm thick) with a mechanical response frequency of 5 MHz. The crystals are 1 inch in diameter with circular chrome/gold electrodes patterned on both sides. The exposed area of the front electrode is around 1.37 cm^2. The area of the graphene layer is 0.64±0.05 cm^2. Figure 5-1 illustrates the steps of the transfer printing process. The graphene layers were synthesized on copper foils by chemical vapor deposition[106]. The copper foils were placed in a quartz chamber and heated to 1050 ^oC under flow of hydrogen gas. To reduce the oxide layer, the samples were annealed for 30 min at 1050 ^oC. After the annealing process, methane gas with a rate of flow of 7 sccm was sent to the chamber for 20 min. The chamber pressure was kept at 200 mTorr during the growth. The growth was terminated by stopping the flow of methane gas and the chamber was cooled back to the room temperature. The graphene coated copper foils were spin coated with a photoresist (PR, AZ5214) with a thickness of 1.4 μm. A flat elastomeric stamp (PDMS) was placed on the PR layer and

the copper foil was etched by 1 M iron chloride solution. After the etching, the PR with graphene layer remains on the PDMS stamp. The stamp was applied on the QCM and heated to 100 ^{o}C to release the graphene-PR layer. Removing the PR layer in acetone provides large area graphene on the surface of QCM.

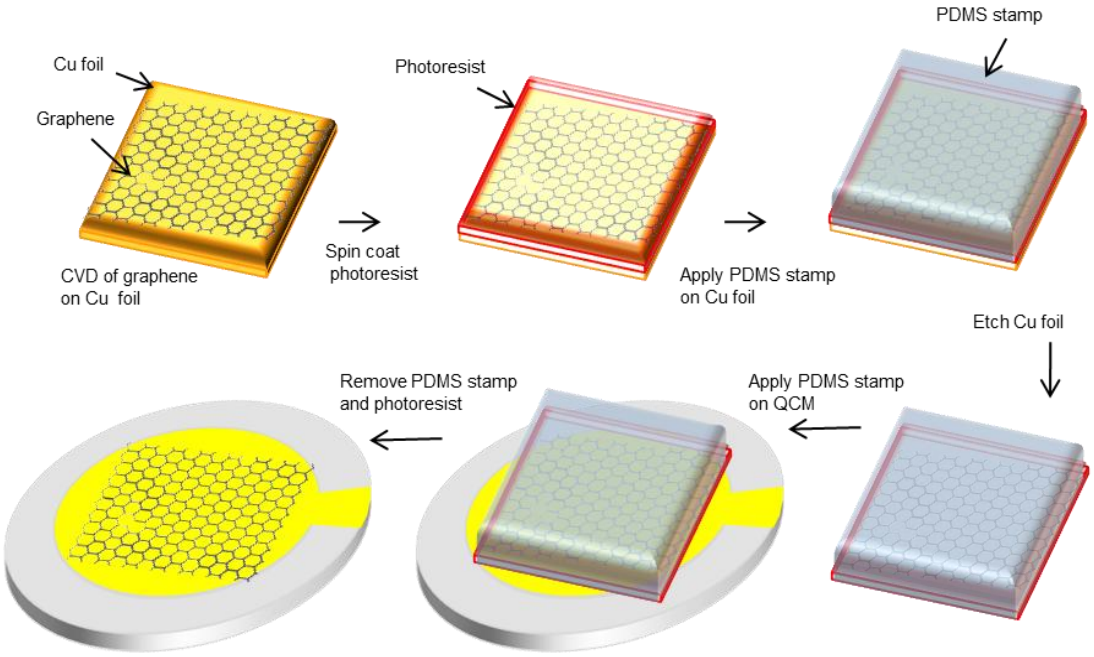

Figure 5-1 Transfer-printing process of graphene on the front electrode of a quartz crystal microbalance.

To obtain the resonance characteristics of the QCM, we measured scattering parameters (S-parameters, S_{11}) of QCM using two-port vector network analyzer (VNA, HP 8753D). S-parameters can elucidate the electromechanical properties of QCM and as well as the interaction of the surrounding medium. Figure 5-2a shows the schematics of the experimental setup. One port of the VNA is connected to the QCM mounted on a crystal holder with a BNC connector. We measured S-parameters for a frequency range of 1 kHz around the resonance frequency of 5MHz. Figure 5-2b shows the phase and magnitude of measured S_{11}. S_{11} shows a clear resonance behavior due to the mechanical resonance of the QCM. At the resonance frequency the magnitude of S_{11} is at a minimum since the total impedance attains its minimum value at the resonance frequency. S_{11} at the resonance is 3 dB less than the off-resonance value. A

steep phase change at the resonance frequency is also a characteristic behavior of an electromechanical resonator. The resonance of quartz crystal has very narrow bandwidth which makes them ideal for frequency measurements. The resonance frequency and the quality factor of the blank QCM are 5,007,323.4 Hz and 22600, respectively. After measuring the S-parameters of the blank QCM, we transfer-printed single layer graphene and measured the S-parameters of graphene coated QCM. The area of transferred graphene is 0.64 cm^2 which is smaller than the area of the front electrode, 1.37 cm^2. The dot lines in Figure 5-2b show the S-parameters of graphene-coated QCM. After the transfer process, the resonance frequency decreases owing to the mass uptake. We observed a frequency change of 20.5 Hz after transferring the graphene layer. The change in the resonance frequency is proportional with the additional mass on QCM which consist of mass of the graphene layer and organic residue due to the transfer process.

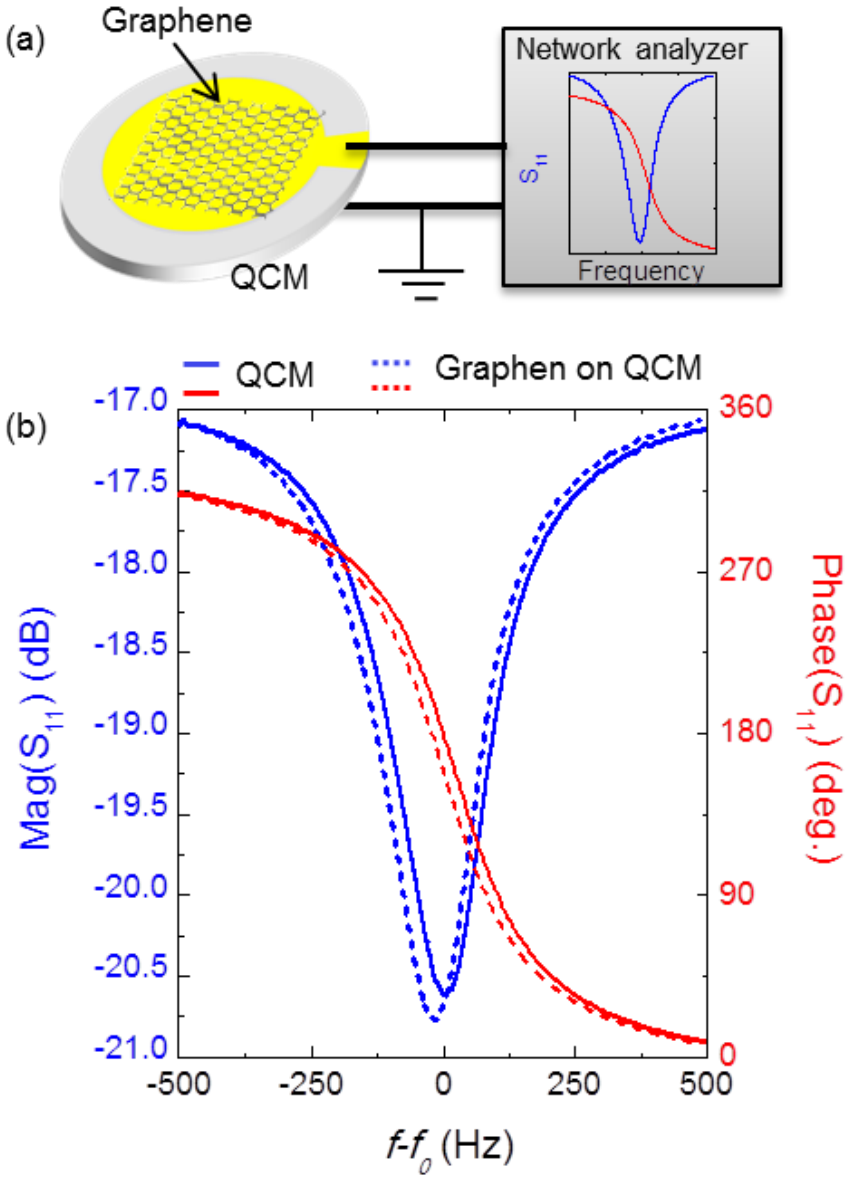

Figure 5-2 (a) Experimental set-up used for probing resonance characteristic of the QCM. A two-port network analyzer is used to measure scattering parameters. (b) Magnitude (blue lines) and phase (red lines) of the measured scattering parameter S_{11} of the port-1, as a function of frequency for blank (solid line) and graphene coated QCM (dot line). The resonance frequency is 5,007,323.4 Hz. The Q-factor of the resonator is around 22600. After coating the surface of QCM with 0.64 cm^2 graphene, we observed around 20 Hz shift in the resonance frequency.

By repeating the transfer-printing of graphene, we were able to obtain multilayer graphene films which allow us to measure the mass density of graphene. Figure 5-3 shows the scattering parameters for a QCM coated with multilayer graphene. The multilayer graphene films were obtained by a sequential transfer printing process. After each transfer process, we measured the scattering parameters. Figures 5-3a and 5-3b show the magnitude and phase of QCM coated with multilayer graphene films. We observed a linear change in the resonance frequency. The scattered plot in Fig3c shows the change of resonance frequency with the layer number. The red line shows the curve obtained by the linear least squares fitting. The slope of the fitting curve provides the interfacial mass change after transfer-printing process. The frequency change of 26 ±2 Hz for each graphene layer is obtained from the fitting curve. It is known that polymer-assistant-transfer-printing process carries some degree of organic residues. We also performed some controlled experiment to quantify the amount of organic residue carried on the QCM.

To quantify the frequency change and mass uptake, we calibrated the QCM by a known amount of mass. A uniform gold film with a thickness of 20nm-measured by an atomic force microscope- was evaporated on QCM with the same area as the graphene sheets. We measured a shift of 4.80 kHz in resonant frequency. The density of the evaporated gold thin film is 16 g/cm^{-3} [121] which corresponds to a mass uptake of 20.5 µg. Since the sensitivity of QCM decreases with the radial distance, we keep the area of the film constant during the calibration. For an exposed area of 0.64 cm^2, the calibration factor is 4.26 ng/Hz. For each graphene layer we obtained 26 Hz frequency shift corresponding a mass uptake of 114 ng. This value includes the mass of both graphene and organic residue. To elucidate the mass of residue, we performed the similar transfer process without growing graphene on copper foils. The observed frequency shift for each transfer process is 8.3 Hz corresponds to a mass uptake of 35ng. After subtracting the mass of residues from the measured mass and normalizing by the area, we estimate the mass density of graphene as 123 ng/cm^2. This value is 35% larger than the theoretical value of 79 ng/cm^2 calculated from the mass density of bulk graphite. This variation is likely because of chemical vapor deposition process which produces

polycrystalline graphene with partial multilayer regions and underestimated mass of organic residues on the graphene or errors in the area of the transferred graphene. There are also other sources of errors related with the calibration procedure such as the thickness and mass density of gold film used for the calibration. We also observed a slight change of band width of QCM likely because of additional interfacial friction between the graphene layers. Figure 5-3d shows the bandwidth of the QCM as a function of graphene layers.

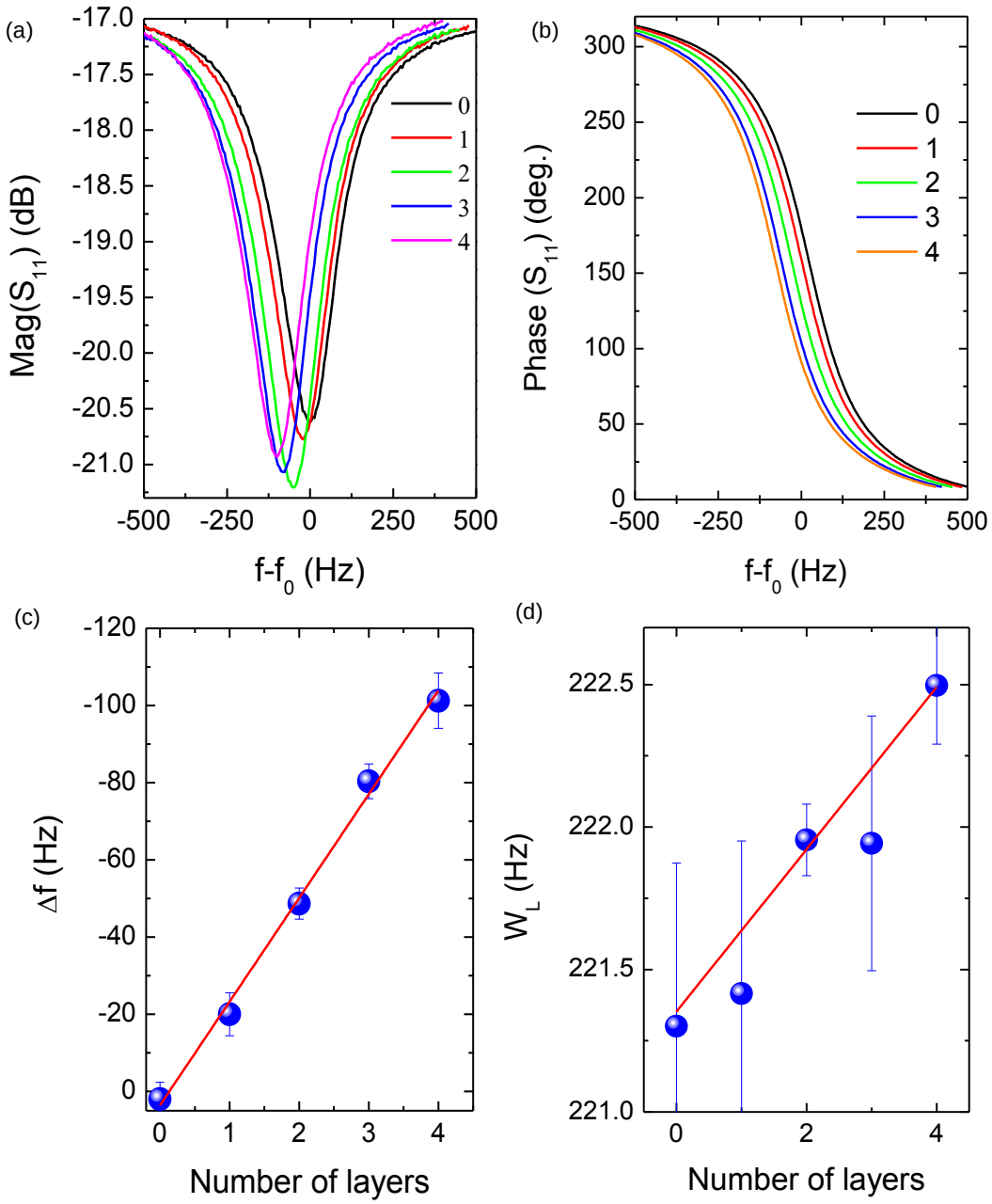

Figure 5-3 Magnitude (a) and phase (b) of scattering parameters measured for QCM coated with multilayer graphene. (c) Measured frequency shift as a function of number of graphene layers. The frequency shift shows a linear dependence on the graphene layers. (d) The bandwidth of the QCM vs. number of graphene layers.

QCM sensors can work in liquid media as well. Integrating the QCM sensor with a flow chamber, we monitored the binding dynamics of proteins on graphene surface from an aqueous solution. We would like to demonstrate that integration of graphene with QCM sensors can be used to probe binding kinetics of organic molecules on graphene surface by means of change of interfacial mass. Figure 5-4a shows schematic representation of the experimental setup used to probe the resonance frequency of the QCM sensor in real time. Quartz crystal is placed in the feedback loop of an oscillator. The time trace of the resonance frequency was monitored by means of a frequency counter. We used a quartz crystal microbalance (Stanford Research, QCM200) integrated with a flow cell. The kinetic parameters of the nonspecific binding on a surface can be extracted from the time trace of the resonance frequency which provides the interfacial mass change. We used 100 nM of Bovine serum albumin (BSA) - a medium size protein-to study nonspecific binding on the surface of bare gold electrode and graphene coated gold electrode. From the time trace of the frequency change, we can obtain the time constant of the binding kinetics. The time constants, obtained by fitting the time trace data, are 390 sec and 30 sec, for bare QCM and graphene coated QCM, respectively. From the measured the time constants, we can estimate the association constants of BSA on bare gold surface and graphene coated gold surface as 0.26 $M^{-1}sec^{-1}$ and 3.3 $M^{-1}sec^{-1}$, respectively. There is a significant increase in the association constant likely because of hydrophobic nature of the graphene surface.

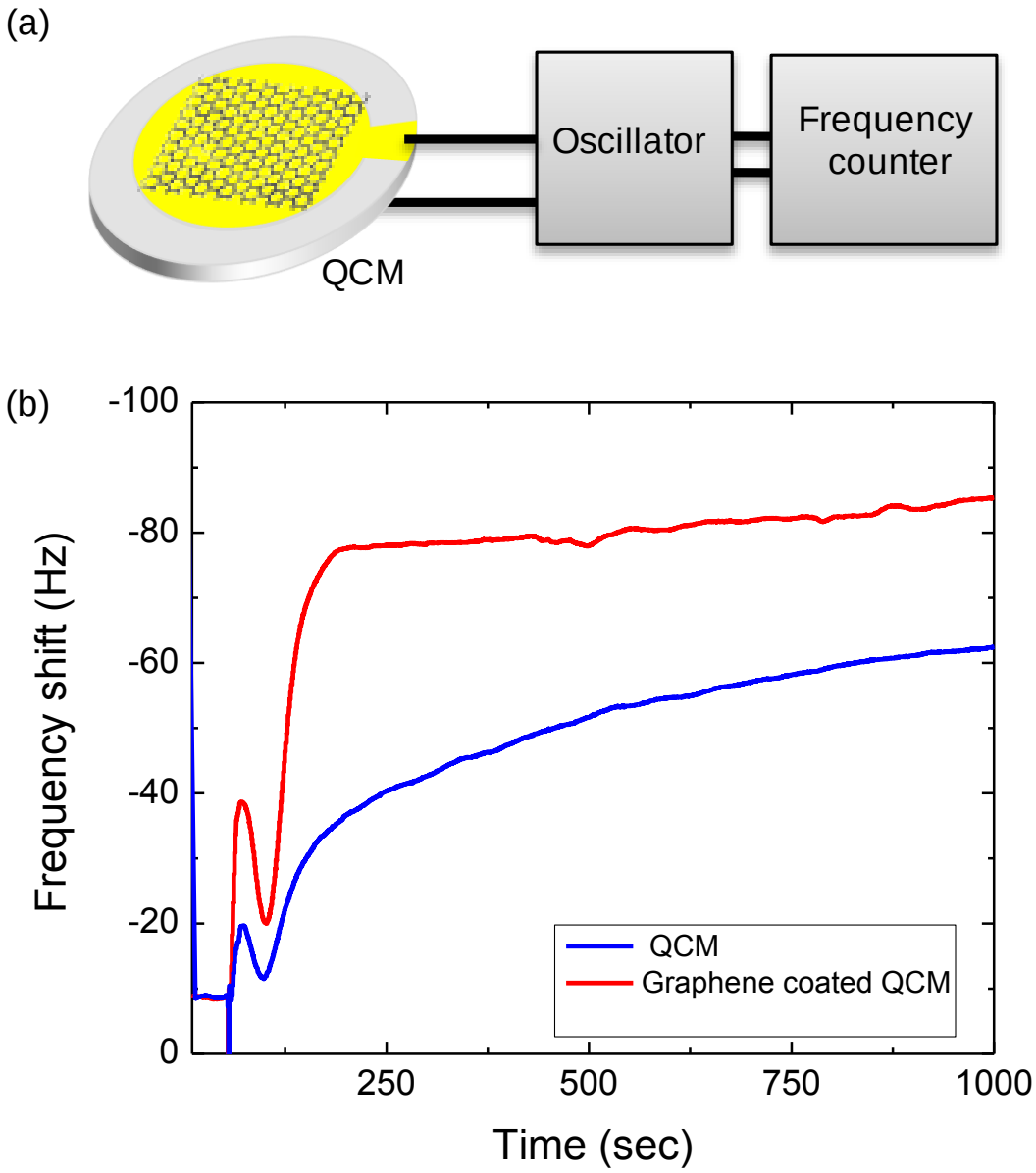

Figure 5-4(a) Schematics of the experimental setup used to probe the time trace of the resonance frequency of the QCM. (b) Overlaid time trace of resonance frequency indicating the binding kinetics of Bovine serum albumin (BSA) proteins on the bare QCM surface and graphene coated QCM surface. The concentration of BSA is 100nM.

Mass detection can also be used for monitoring chemical reactions on graphene surfaces. We would like to trace oxidation of the graphene surface by monitoring the interfacial mass change and correlate the mass change with Raman spectra. The graphene structure undergoes chemical variations as it is exposed to mild oxygen plasma. After transfer-printing the graphene layers on a QCM, we exposed the surface to mild oxygen plasma in a reactive ion etching chamber. After each short exposure time, we measured the change in the resonance frequency of the QCM. Figure 5-5 exhibits the change of the resonant frequency and correlated mass uptake associated with the oxidation of the graphene surface. We performed the exposure of plasma until complete etching of the graphene layer. To correlate the mass uptake and the crystal structure of the graphene layer, we measured the Raman spectra of graphene after each exposure. Figure 5-5 (b) shows the recorded Raman spectra for various exposure times. We observed three different regimes, for the first 10 sec. interfacial mass increases by 93 ng/cm^2. This mass uptake is likely due to the oxidation of the graphene layer. This oxidation can also be seen from the Raman spectra. The increase of the intensity of the D-band (1950 cm^{-1}) confirms the formation of sp bonds and associated lattice distortion. The decrease in the intensity of 2D-band (2700 cm^{-1}) shows deformation of the crystal structure of graphene. After 15 sec. of expose we observed a decrease in the interfacial mass. This decrease could be because of CO_2 release which is expected for early stage of graphene oxidation. As we further increase the exposure time, we observed complete removal of the graphene layer. This step could include physical removing of small graphene/graphene oxide flakes because of bombarding of the surface by energetic oxygen atoms. Correlating the interfacial mass change and Raman spectra could provide more inside for understanding the interfacial reaction of graphene surface.

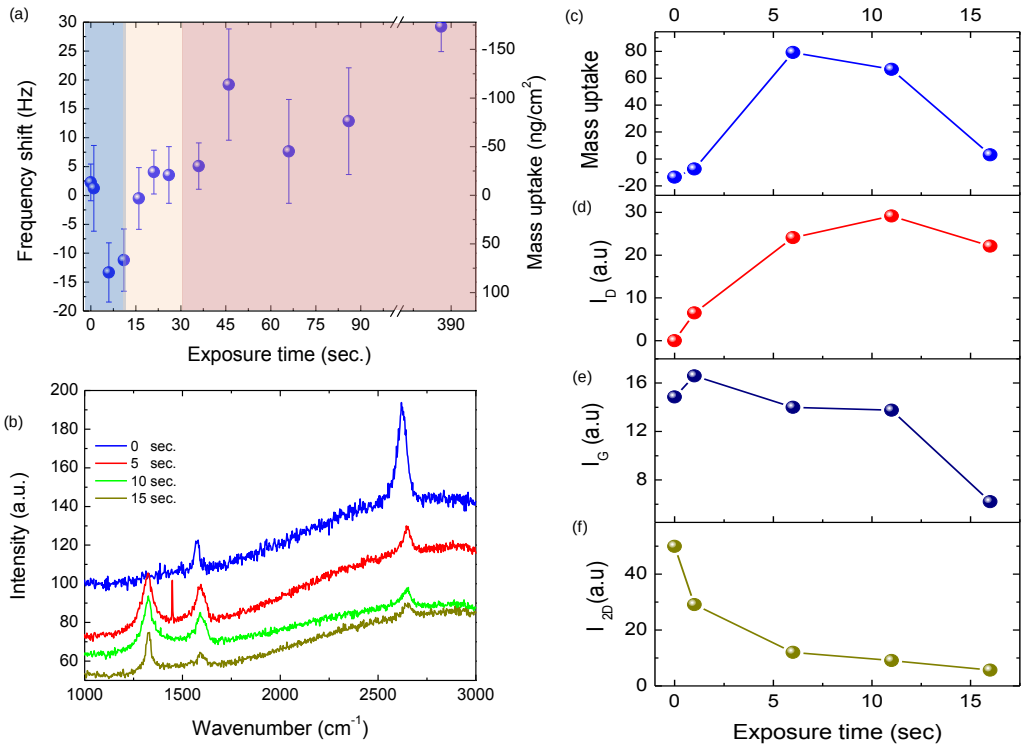

Figure 5-5 Probing oxidation of graphene by mass detection. (a) Change of the resonant frequency and associated mass uptake of graphene exposed to mild oxygen plasma. (b) Raman spectra of graphene with various exposure times. (c-f) Mass uptake of graphene and correlated with Raman intensity for D, G and 2D bands.

Chapter 6

Summary and future work

In this thesis, we used SWNT networks and single layer graphene as model materials to understand interfacial process on graphitic carbon surface. In the first part of the thesis, we synthesized SWNT networks by chemical vapor deposition and transfer-printed on gold surfaces. We studied the excitation of surface plasmon-polaritons on nanotube coated gold surfaces with sub-monolayer, monolayer, and multilayer surface coverage. Integrating the fabricated sensor with a microfluidic device, we were able to obtain binding dynamics of a bovine serum albumin (BSA) protein on SWNT networks with various tube densities. The results reveal the kinetic parameters for nonspecific binding of BSA on SWNT surface for various tube densities. In the second part of the thesis, graphene layers were synthesized by chemical vapor deposition on copper foils and transfer-printed on a quartz crystal microbalance (QCM). Probing the mechanical resonance of the QCM, we were able to measure mass density of single layer graphene. We extended the developed technique to probe binding dynamics of proteins on graphene surface. We obtained association constant of nonspecific binding of BSA on graphene surface from an aqueous solution. The presence of graphene layer increases the nonspecific binding likely because of the hydrophobic nature of graphitic carbon. Furthermore, we monitored oxidation of graphene surface under oxygen plasma by tracing the changes of interfacial mass of the graphene layer. During the oxidation of graphene, by monitoring the mass change and change of Raman spectra, we observed three regimes, (1) formation of graphene oxide which increases the interfacial mass, (2) release of CO_2 and (3) removal of small graphene/graphene oxide flakes.

Further studies must be done to fully understand the adsorption of organic molecules on carbon surface. In this study we provide a proof-of-principle demonstration of two different methods based on optical and mass detection. We would like continue this work by studying adsorption of small molecules on SWNT and graphene surface from gas phase and aqueous solution. We anticipate that with the help of these techniques, we can understand the fundamental interaction on carbon surface at the molecular level.

Bibliography:

[1] S. Iijima, "Helical Microtubules of Graphitic Carbon," *Nature,* vol. 354, pp. 56-58, Nov 7 1991.

[2] A. K. Geim and K. S. Novoselov, "The rise of graphene," *Nature Materials,* vol. 6, pp. 183-191, 2007.

[3] T. Masciangioli and W. X. Zhang, "Environmental technologies at the nanoscale," *Environ Sci Technol,* vol. 37, pp. 102a-108a, Mar 1 2003.

[4] D. Tasis, N. Tagmatarchis, A. Bianco, and M. Prato, "Chemistry of carbon nanotubes," *Chemical Reviews,* vol. 106, pp. 1105-1136, Mar 2006.

[5] W. R. Yang, K. R. Ratinac, S. P. Ringer, P. Thordarson, J. J. Gooding, and F. Braet, "Carbon Nanomaterials in Biosensors: Should You Use Nanotubes or Graphene?," *Angewandte Chemie-International Edition,* vol. 49, pp. 2114-2138, 2010.

[6] C. Wang, A. Badmaev, A. Jooyaie, M. Q. Bao, K. L. Wang, K. Galatsis, and C. W. Zhou, "Radio Frequency and Linearity Performance of Transistors Using High-Purity Semiconducting Carbon Nanotubes," *Acs Nano,* vol. 5, pp. 4169-4176, May 2011.

[7] E. Pince and C. Kocabas, "Investigation of high frequency performance limit of graphene field effect transistors," *Applied Physics Letters,* vol. 97, Oct 25 2010.

[8] Y. M. Lin, A. Valdes-Garcia, S. J. Han, D. B. Farmer, I. Meric, Y. N. Sun, Y. Q. Wu, C. Dimitrakopoulos, A. Grill, P. Avouris, and K. A. Jenkins, "Wafer-Scale Graphene Integrated Circuit," *Science,* vol. 332, pp. 1294-1297, Jun 10 2011.

[9] C. Kocabas, H. S. Kim, T. Banks, J. A. Rogers, A. A. Pesetski, J. E. Baumgardner, S. V. Krishnaswamy, and H. Zhang, "Radio frequency analog electronics based on carbon nanotube transistors," *Proc Natl Acad Sci U S A,* vol. 105, pp. 1405-9, Feb 5 2008.

[10] S. J. Kang, C. Kocabas, T. Ozel, M. Shim, N. Pimparkar, M. A. Alam, S. V. Rotkin, and J. A. Rogers, "High-performance electronics using dense, perfectly aligned arrays of single-walled carbon nanotubes," *Nat Nanotechnol,* vol. 2, pp. 230-6, Apr 2007.

[11] C. Rutherglen, D. Jain, and P. Burke, "Nanotube electronics for radiofrequency applications," *Nat Nanotechnol,* vol. 4, pp. 811-9, Dec 2009.

[12] J. P. Hill, W. Jin, A. Kosaka, T. Fukushima, H. Ichihara, T. Shimomura, K. Ito, T. Hashizume, N. Ishii, and T. Aida, "Self-assembled hexa-peri-hexabenzocoronene graphitic nanotube," *Science,* vol. 304, pp. 1481-3, Jun 4 2004.

[13] Y. Zhao and D. G. Truhlar, "Size-selective supramolecular chemistry in a hydrocarbon nanoring," *J Am Chem Soc,* vol. 129, pp. 8440-+, Jul 11 2007.

[14] S. Grimme, J. Antony, T. Schwabe, and C. Muck-Lichtenfeld, "Density functional theory with dispersion corrections for supramolecular structures, aggregates, and complexes of (bio)organic molecules," *Organic & Biomolecular Chemistry,* vol. 5, pp. 741-758, 2007.

[15] J. Kong, N. R. Franklin, C. W. Zhou, M. G. Chapline, S. Peng, K. J. Cho, and H. J. Dai, "Nanotube molecular wires as chemical sensors," *Science,* vol. 287, pp. 622-625, Jan 28 2000.

[16] B. L. Allen, P. D. Kichambare, and A. Star, "Carbon nanotube field-effect-transistor-based biosensors," *Advanced Materials,* vol. 19, pp. 1439-1451, Jun 4 2007.

[17] O. Salihoglu, S. Balci, and C. Kocabas, "Plasmon-polaritons on graphene-metal surface and their use in biosensors," *Applied Physics Letters,* vol. 100, May 21 2012.

[18] O. Gulseren, T. Yildirim, and S. Ciraci, "Tunable adsorption on carbon nanotubes," *Phys Rev Lett,* vol. 87, p. 116802, Sep 10 2001.

[19] E. Durgun, S. Dag, V. M. K. Bagci, O. Gulseren, T. Yildirim, and S. Ciraci, "Systematic study of adsorption of single atoms on a carbon nanotube," *Physical Review B,* vol. 67, May 15 2003.

[20] E. Durgun, S. Dag, S. Ciraci, and O. Gulseren, "Energetics and electronic structures of individual atoms adsorbed on carbon nanotubes," *Journal of Physical Chemistry B,* vol. 108, pp. 575-582, Jan 15 2004.

[21] P. A. Denis and F. Iribarne, "Thiophene adsorption on Single Wall Carbon Nanotubes and graphene," *Journal of Molecular Structure-Theochem,* vol. 957, pp. 114-119, Oct 15 2010.

[22] S. B. Fagan, A. G. Souza, J. O. G. Lima, J. Mendes, O. P. Ferreira, I. O. Mazali, O. L. Alves, and M. S. Dresselhaus, "1,2-dichlorobenzene interacting with carbon nanotubes," *Nano Letters,* vol. 4, pp. 1285-1288, Jul 2004.

[23] L. L. Wang, D. Q. Zhu, L. Duan, and W. Chen, "Adsorption of single-ringed N- and S-heterocyclic aromatics on carbon nanotubes," *Carbon,* vol. 48, pp. 3906-3915, Nov 2010.

[24] B. Pan and B. S. Xing, "Adsorption Mechanisms of Organic Chemicals on Carbon Nanotubes," *Environ Sci Technol,* vol. 42, pp. 9005-9013, Dec 15 2008.

[25] K. Yang, X. L. Wang, L. Z. Zhu, and B. S. Xing, "Competitive sorption of pyrene, phenanthrene, and naphthalene on multiwalled carbon nanotubes," *Environ Sci Technol,* vol. 40, pp. 5804-5810, Sep 15 2006.

[26] E. S. Alldredge, S. C. Badescu, N. Bajwa, F. K. Perkins, E. S. Snow, T. L. Reinecke, J. L. Passmore, and Y. L. Chang, "Adsorption of linear chain molecules on carbon nanotubes," *Physical Review B,* vol. 78, Oct 2008.

[27] K. Yang, X. Wang, L. Zhu, and B. Xing, "Competitive sorption of pyrene, phenanthrene, and naphthalene on multiwalled carbon nanotubes," *Environ Sci Technol,* vol. 40, pp. 5804-10, Sep 15 2006.

[28] S. Debnath, Q. H. Cheng, T. G. Hedderman, and H. J. Byrne, "Comparative Study of the Interaction of Different Polycyclic Aromatic Hydrocarbons on Different Types of Single-Walled Carbon Nanotubes," *Journal of Physical Chemistry C,* vol. 114, pp. 8167-8175, May 13 2010.

[29] A. Patrykiejew, M. Jaroniec, and A. W. Marczewski, "Partially Mobile and Partially Localized Monolayer Films of Gases on Solid-Surfaces .5. Application of the Model to Adsorption of Simple Gases on Graphite and Boron-Nitride," *Thin Solid Films,* vol. 76, pp. 247-258, 1981.

[30] E. Castillejos, B. Bachiller-Baeza, I. Rodriguez-Ramos, and A. Guerrero-Ruiz, "An immersion calorimetry study of the interaction of organic compounds with carbon nanotube surfaces," *Carbon,* vol. 50, pp. 2731-2740, Jul 2012.

[31] F. Schedin, A. K. Geim, S. V. Morozov, E. W. Hill, P. Blake, M. I. Katsnelson, and K. S. Novoselov, "Detection of individual gas molecules adsorbed on graphene," *Nature Materials,* vol. 6, pp. 652-655, Sep 2007.

[32] P. W. Barone, S. Baik, D. A. Heller, and M. S. Strano, "Near-infrared optical sensors based on single-walled carbon nanotubes," *Nature Materials,* vol. 4, pp. 86-U16, Jan 2005.

[33] P. G. Collins, K. Bradley, M. Ishigami, and A. Zettl, "Extreme oxygen sensitivity of electronic properties of carbon nanotubes," *Science,* vol. 287, pp. 1801-1804, Mar 10 2000.

[34] E. S. Snow, F. K. Perkins, E. J. Houser, S. C. Badescu, and T. L. Reinecke, "Chemical detection with a single-walled carbon nanotube capacitor," *Science,* vol. 307, pp. 1942-1945, Mar 25 2005.

[35] Q. Zhao, Z. H. Gan, and Q. K. Zhuang, "Electrochemical sensors based on carbon nanotubes," *Electroanalysis,* vol. 14, pp. 1609-1613, Dec 2002.

[36] S. Ghosh, A. K. Sood, and N. Kumar, "Carbon nanotube flow sensors," *Science,* vol. 299, pp. 1042-1044, Feb 14 2003.

[37] G. H. Liu, J. L. Wang, Y. F. Zhu, and X. R. Zhang, "Application of multiwalled carbon nanotubes as a solid-phase extraction sorbent for chlorobenzenes," *Analytical Letters,* vol. 37, pp. 3085-3104, Nov 2004.

[38] K. Pyrzynska, A. Stafiej, and M. Biesaga, "Sorption behavior of acidic herbicides on carbon nanotubes," *Microchimica Acta,* vol. 159, pp. 293-298, Jul 2007.

[39] S. G. Wang, X. W. Liu, W. X. Gong, W. Nie, B. Y. Gao, and Q. Y. Yue, "Adsorption of fulvic acids from aqueous solutions by carbon nanotubes,"

Journal of Chemical Technology and Biotechnology, vol. 82, pp. 698-704, Aug 2007.

[40] S. Agnihotri, M. J. Rood, and M. Rostam-Abadi, "Adsorption equilibrium of organic vapors on single-walled carbon nanotubes," *Carbon,* vol. 43, pp. 2379-2388, Sep 2005.

[41] F. S. Su and C. S. Lu, "Adsorption kinetics, thermodynamics and desorption of natural dissolved organic matter by multiwalled carbon nanotubes," *Journal of Environmental Science and Health Part a-Toxic/Hazardous Substances & Environmental Engineering,* vol. 42, pp. 1543-1552, 2007.

[42] S. Y. Brichka, L. A. Belyakova, G. P. Prikhod'ko, and N. V. Roik, "Surface structure and adsorption properties of multiwalled carbon nanotubes," *Russian Chemical Bulletin,* vol. 55, pp. 1775-1779, Oct 2006.

[43] C. S. Lu, Y. L. Chung, and K. F. Chang, "Adsorption thermodynamic and kinetic studies of trihalomethanes on multiwalled carbon nanotubes," *Journal of Hazardous Materials,* vol. 138, pp. 304-310, Nov 16 2006.

[44] J. Hilding, E. A. Grulke, S. B. Sinnott, D. L. Qian, R. Andrews, and M. Jagtoyen, "Sorption of butane on carbon multiwall nanotubes at room temperature," *Langmuir,* vol. 17, pp. 7540-7544, Nov 27 2001.

[45] X. M. Yan, B. Y. Shi, J. J. Lu, C. H. Feng, D. S. Wang, and H. X. Tang, "Adsorption and desorption of atrazine on carbon nanotubes," *Journal of Colloid and Interface Science,* vol. 321, pp. 30-38, May 1 2008.

[46] K. Yang, L. Z. Zhu, and B. S. Xing, "Adsorption of polycyclic aromatic hydrocarbons by carbon nanomaterials," *Environ Sci Technol,* vol. 40, pp. 1855-1861, Mar 15 2006.

[47] Y. H. Shih and M. S. Li, "Adsorption of selected volatile organic vapors on multiwall carbon nanotubes," *Journal of Hazardous Materials,* vol. 154, pp. 21-28, Jun 15 2008.

[48] J. J. Zhao, A. Buldum, J. Han, and J. P. Lu, "Gas molecule adsorption in carbon nanotubes and nanotube bundles," *Nanotechnology,* vol. 13, pp. 195-200, Apr 2002.

[49] K. Yang and B. S. Xing, "Desorption of polycyclic aromatic hydrocarbons from carbon nanomaterials in water," *Environmental Pollution,* vol. 145, pp. 529-537, Jan 2007.

[50] P. L. Ferguson, G. T. Chandler, R. C. Templeton, A. Demarco, W. A. Scrivens, and B. A. Englehart, "Influence of sediment-amendment with single-walled carbon nanotubes and diesel soot on bioaccumulation of hydrophobic organic contaminants by benthic invertebrates," *Environ Sci Technol,* vol. 42, pp. 3879-3885, May 15 2008.

[51] X. Wang, Y. Liu, W. Qiu, and D. Zhu, "Immobilization of tetra-tert-butylphthalocyanines on carbon nanotubes: a first step towards the development of new nanomaterials," *Journal of Materials Chemistry,* vol. 12, pp. 1636-1639, 2002.

[52] M. Shim, N. W. S. Kam, R. J. Chen, Y. M. Li, and H. J. Dai, "Functionalization of carbon nanotubes for biocompatibility and biomolecular recognition," *Nano Letters,* vol. 2, pp. 285-288, Apr 2002.

[53] J. W. Lee, H. C. Kang, W. G. Shim, C. Kim, and H. Moon, "Methane adsorption on multi-walled carbon nanotube at (303.15, 313.15, and 323.15) K," *Journal of Chemical and Engineering Data,* vol. 51, pp. 963-967, May 11 2006.

[54] M. Sander, Y. F. Lu, and J. J. Pignatello, "A thermodynamically based method to quantify true sorption hysteresis," *Journal of Environmental Quality,* vol. 34, pp. 1063-1072, May-Jun 2005.

[55] W. Chen, L. Duan, and D. Q. Zhu, "Adsorption of polar and nonpolar organic chemicals to carbon nanotubes," *Environ Sci Technol,* vol. 41, pp. 8295-8300, Dec 15 2007.

[56] H. H. Cho, B. A. Smith, J. D. Wnuk, D. H. Fairbrother, and W. P. Ball, "Influence of surface oxides on the adsorption of naphthalene onto multiwalled carbon nanotubes," *Environ Sci Technol,* vol. 42, pp. 2899-2905, Apr 15 2008.

[57] B. Pan, D. H. Lin, H. Mashayekhi, and B. S. Xing, "Adsorption and hysteresis of bisphenol A and 17 alpha-ethinyl estradiol on carbon nanomaterials," *Environ Sci Technol,* vol. 42, pp. 5480-5485, Aug 1 2008.

[58] D. Crespo and R. T. Yang, "Adsorption of organic vapors on single-walled carbon nanotubes," *Industrial & Engineering Chemistry Research,* vol. 45, pp. 5524-5530, Aug 2 2006.

[59] Z. G. Mao and S. B. Sinnott, "A computational study of molecular diffusion and dynamic flow through carbon nanotubes," *Journal of Physical Chemistry B,* vol. 104, pp. 4618-4624, May 18 2000.

[60] F. Tournus and J. C. Charlier, "Ab initio study of benzene adsorption on carbon nanotubes," *Physical Review B,* vol. 71, Apr 2005.

[61] S. Gotovac, C. M. Yang, Y. Hattori, K. Takahashi, H. Kanoh, and K. Kaneko, "Adsorption of polyaromatic hydrocarbons on single wall carbon nanotubes of different functionalities and diameters," *Journal of Colloid and Interface Science,* vol. 314, pp. 18-24, Oct 1 2007.

[62] J. J. Davis, M. L. H. Green, H. A. O. Hill, Y. C. Leung, P. J. Sadler, J. Sloan, A. V. Xavier, and S. C. Tsang, "The immobilisation of proteins in carbon nanotubes," *Inorganica Chimica Acta,* vol. 272, pp. 261-266, May 1 1998.

[63] J. M. Hilding and E. A. Grulke, "Heat of adsorption of butane on multiwalled carbon nanotubes," *Journal of Physical Chemistry B,* vol. 108, pp. 13688-13695, Sep 9 2004.

[64] X. J. Peng, Y. H. Li, Z. K. Luan, Z. C. Di, H. Y. Wang, B. H. Tian, and Z. P. Jia, "Adsorption of 1,2-dichlorobenzene from water to carbon nanotubes," *Chemical Physics Letters,* vol. 376, pp. 154-158, Jul 17 2003.

[65] L. Y. Piao, Q. R. Liu, Y. D. Li, and C. Wang, "Adsorption of L-phenylalanine on single-walled carbon nanotubes," *Journal of Physical Chemistry C,* vol. 112, pp. 2857-2863, Feb 28 2008.

[66] G. Onyestyak, Z. Otvos, J. Valyon, I. Kiricsi, and L. V. C. Rees, "Acetylene sorption dynamics in carbon nanotubes," *Helvetica Chimica Acta,* vol. 87, pp. 1508-1514, 2004.

[67] Q. Liao, J. Sun, and L. Gao, "The adsorption of resorcinol from water using multi-walled carbon nanotubes," *Colloids and Surfaces a-Physicochemical and Engineering Aspects,* vol. 312, pp. 160-165, Jan 15 2008.

[68] G. Zhou, W. H. Duan, and B. L. Gu, "First-principles study on morphology and mechanical properties of single-walled carbon nanotube," *Chemical Physics Letters,* vol. 333, pp. 344-349, Jan 19 2001.

[69] C. S. Lu, Y. L. Chung, and K. F. Chang, "Adsorption of trihalomethanes from water with carbon nanotubes," *Water Research,* vol. 39, pp. 1183-1189, Mar 2005.

[70] R. Q. Long and R. T. Yang, "Carbon nanotubes as superior sorbent for dioxin removal," *J Am Chem Soc,* vol. 123, pp. 2058-2059, Mar 7 2001.

[71] O. Gulseren, T. Yildirim, and S. Ciraci, "Systematic ab initio study of curvature effects in carbon nanotubes," *Physical Review B,* vol. 65, Apr 15 2002.

[72] M. S. Dresselhaus, G. Dresselhaus, J. C. Charlier, and E. Hernandez, "Electronic, thermal and mechanical properties of carbon nanotubes," *Philosophical Transactions of the Royal Society a-Mathematical Physical and Engineering Sciences,* vol. 362, pp. 2065-2098, Oct 15 2004.

[73] M. S. Dresselhaus, G. Dresselhaus, and P. Avouris, *Carbon nanotubes : synthesis, structure, properties, and applications*. Berlin ; New York: Springer, 2001.

[74] A. K. Geim, "Graphene: Status and Prospects," *Science,* vol. 324, pp. 1530-1534, Jun 19 2009.

[75] L. D. Landau, E. M. Lifshi͡ts, and L. P. Pitaevskiĭ, *Statistical physics*. Oxford ; New York: Pergamon Press, 1980.

[76] N. D. Mermin, "Crystalline Order in Two Dimensions," *Physical Review,* vol. 176, pp. 250-254, 1968.

[77] F. H. L. Koppens, D. E. Chang, and F. J. G. de Abajo, "Graphene Plasmonics: A Platform for Strong Light-Matter Interactions," *Nano Letters,* vol. 11, pp. 3370-3377, Aug 2011.

[78] K. S. Novoselov, Z. Jiang, Y. Zhang, S. V. Morozov, H. L. Stormer, U. Zeitler, J. C. Maan, G. S. Boebinger, P. Kim, and A. K. Geim, "Room-temperature quantum hall effect in graphene," *Science,* vol. 315, pp. 1379-1379, Mar 9 2007.

[79] K. S. Novoselov, E. McCann, S. V. Morozov, V. I. Fal'ko, M. I. Katsnelson, U. Zeitler, D. Jiang, F. Schedin, and A. K. Geim, "Unconventional quantum Hall effect and Berry's phase of 2 pi in bilayer graphene," *Nature Physics,* vol. 2, pp. 177-180, Mar 2006.

[80] A. H. Castro Neto, F. Guinea, N. M. R. Peres, K. S. Novoselov, and A. K. Geim, "The electronic properties of graphene," *Reviews of Modern Physics,* vol. 81, pp. 109-162, Jan-Mar 2009.

[81] E. Dervishi, Z. R. Li, Y. Xu, V. Saini, A. R. Biris, D. Lupu, and A. S. Biris, "Carbon Nanotubes: Synthesis, Properties, and Applications," *Particulate Science and Technology,* vol. 27, pp. 107-125, 2009.

[82] C. D. Scott, S. Arepalli, P. Nikolaev, and R. E. Smalley, "Growth mechanisms for single-wall carbon nanotubes in a laser-ablation process," *Applied Physics a-Materials Science & Processing,* vol. 72, pp. 573-580, May 2001.

[83] Y. Ando and X. L. Zhao, "Synthesis of carbon nanotubes by arc-discharge method," *New Diamond and Frontier Carbon Technology,* vol. 16, pp. 123-137, 2006.

[84] M. Terrones, "Carbon nanotubes: synthesis and properties, electronic devices and other emerging applications," *International Materials Reviews,* vol. 49, pp. 325-377, Dec 2004.

[85] M. J. Bronikowski, P. A. Willis, D. T. Colbert, K. A. Smith, and R. E. Smalley, "Gas-phase production of carbon single-walled nanotubes from carbon monoxide via the HiPco process: A parametric study," *Journal of Vacuum Science & Technology a-Vacuum Surfaces and Films,* vol. 19, pp. 1800-1805, Jul-Aug 2001.

[86] P. Nikolaev, "Gas-phase production of single-walled carbon nanotubes from carbon monoxide: A review of the HiPco process," *Journal of Nanoscience and Nanotechnology,* vol. 4, pp. 307-316, Apr 2004.

[87] C. H. Song, P. E. Pehrsson, and W. Zhao, "Optical enzymatic detection of glucose based on hydrogen peroxide-sensitive HiPco carbon nanotubes," *Journal of Materials Research,* vol. 21, pp. 2817-2823, Nov 2006.

[88] A. M. Cassell, J. A. Raymakers, J. Kong, and H. J. Dai, "Large scale CVD synthesis of single-walled carbon nanotubes," *Journal of Physical Chemistry B,* vol. 103, pp. 6484-6492, Aug 5 1999.

[89] J. Kong, A. M. Cassell, and H. J. Dai, "Chemical vapor deposition of methane for single-walled carbon nanotubes," *Chemical Physics Letters,* vol. 292, pp. 567-574, Aug 14 1998.

[90] A. Moisala, A. G. Nasibulin, and E. I. Kauppinen, "The role of metal nanoparticles in the catalytic production of single-walled carbon nanotubes - a review," *Journal of Physics-Condensed Matter,* vol. 15, pp. S3011-S3035, Oct 29 2003.

[91] M. Meyyappan, *Carbon nanotubes : science and applications*. Boca Raton, FL: CRC Press, 2005.

[92] P. Nikolaev, M. J. Bronikowski, R. K. Bradley, F. Rohmund, D. T. Colbert, K. A. Smith, and R. E. Smalley, "Gas-phase catalytic growth of single-walled carbon nanotubes from carbon monoxide," *Chemical Physics Letters,* vol. 313, pp. 91-97, Nov 5 1999.

[93] H. J. Dai, "Carbon nanotubes: opportunities and challenges," *Surface Science,* vol. 500, pp. 218-241, Mar 10 2002.

[94] X. S. Li, W. W. Cai, L. Colombo, and R. S. Ruoff, "Evolution of Graphene Growth on Ni and Cu by Carbon Isotope Labeling," *Nano Letters,* vol. 9, pp. 4268-4272, Dec 2009.

[95] C. L. Cheung, A. Kurtz, H. Park, and C. M. Lieber, "Diameter-controlled synthesis of carbon nanotubes," *Journal of Physical Chemistry B,* vol. 106, pp. 2429-2433, Mar 14 2002.

[96] S. P. O'Brien, L. M. Huang, and S. Wind, "Controlled growth of single walled carbon nanotube assemblies from thin film mesoporous silica templates.," *Abstracts of Papers of the American Chemical Society,* vol. 226, pp. U766-U766, Sep 2003.

[97] H. J. Dai, "Carbon nanotubes: Synthesis, integration, and properties," *Accounts of Chemical Research,* vol. 35, pp. 1035-1044, Dec 2002.

[98] M. S. Dresselhaus, A. Jorio, M. Hofmann, G. Dresselhaus, and R. Saito, "Perspectives on Carbon Nanotubes and Graphene Raman Spectroscopy," *Nano Letters,* vol. 10, pp. 751-758, Mar 2010.

[99] M. S. Dresselhaus, G. Dresselhaus, A. Jorio, A. G. Souza, and R. Saito, "Raman spectroscopy on isolated single wall carbon nanotubes," *Carbon,* vol. 40, pp. 2043-2061, 2002.

[100] P. C. Eklund, J. M. Holden, and R. A. Jishi, "Vibrational-Modes of Carbon Nanotubes - Spectroscopy and Theory," *Carbon,* vol. 33, pp. 959-972, 1995.

[101] B. Lang, "A LEED study of the deposition of carbon on platinum crystal surfaces," *Surface Science,* vol. 53, pp. 317-329, 1975.

[102] W. Choi, I. Lahiri, R. Seelaboyina, and Y. S. Kang, "Synthesis of Graphene and Its Applications: A Review," *Critical Reviews in Solid State and Materials Sciences,* vol. 35, pp. 52-71, 2010.

[103] A. J. Van Bommel, J. E. Crombeen, and A. Van Tooren, "LEED and Auger electron observations of the SiC(0001) surface," *Surface Science,* vol. 48, pp. 463-472, 1975.

[104] C. Berger, Z. M. Song, T. B. Li, X. B. Li, A. Y. Ogbazghi, R. Feng, Z. T. Dai, A. N. Marchenkov, E. H. Conrad, P. N. First, and W. A. de Heer, "Ultrathin epitaxial graphite: 2D electron gas properties and a route toward graphene-based nanoelectronics," *Journal of Physical Chemistry B,* vol. 108, pp. 19912-19916, Dec 30 2004.

[105] J. Hass, W. A. de Heer, and E. H. Conrad, "The growth and morphology of epitaxial multilayer graphene," *Journal of Physics-Condensed Matter,* vol. 20, Aug 13 2008.

[106] L. Colombo, X. S. Li, W. W. Cai, J. H. An, S. Kim, J. Nah, D. X. Yang, R. Piner, A. Velamakanni, I. Jung, E. Tutuc, S. K. Banerjee, and R. S. Ruoff, "Large-Area Synthesis of High-Quality and Uniform Graphene Films on Copper Foils," *Science,* vol. 324, pp. 1312-1314, Jun 5 2009.

[107] D. C. Wei and Y. Q. Liu, "Controllable Synthesis of Graphene and Its Applications," *Advanced Materials,* vol. 22, pp. 3225-3241, Aug 10 2010.

[108] Q. K. Yu, J. Lian, S. Siriponglert, H. Li, Y. P. Chen, and S. S. Pei, "Graphene segregated on Ni surfaces and transferred to insulators," *Applied Physics Letters,* vol. 93, Sep 15 2008.

[109] A. Reina, X. T. Jia, J. Ho, D. Nezich, H. B. Son, V. Bulovic, M. S. Dresselhaus, and J. Kong, "Layer Area, Few-Layer Graphene Films on Arbitrary Substrates by Chemical Vapor Deposition," *Nano Letters,* vol. 9, pp. 3087-3087, Aug 2009.

[110] M. Eizenberg and J. M. Blakely, "Carbon monolayer phase condensation on Ni(111)," *Surface Science,* vol. 82, pp. 228-236, 1979.

[111] X. S. Li, W. W. Cai, J. H. An, S. Kim, J. Nah, D. X. Yang, R. Piner, A. Velamakanni, I. Jung, E. Tutuc, S. K. Banerjee, L. Colombo, and R. S. Ruoff, "Large-Area Synthesis of High-Quality and Uniform Graphene Films on Copper Foils," *Science,* vol. 324, pp. 1312-1314, Jun 5 2009.

[112] S. A. Maier, *Plasmonics : fundamentals and applications*. New York: Springer, 2007.

[113] L. Novotny and B. Hecht, *Principles of nano-optics*. Cambridge ; New York: Cambridge University Press, 2006.

[114] J. i. Homola and J. Dostálek, *Surface plasmon resonance based sensors*. Berlin ; New York: Springer, 2006.

[115] T. Oznuluer, E. Pince, E. O. Polat, O. Balci, O. Salihoglu, and C. Kocabas, "Synthesis of graphene on gold," *Applied Physics Letters,* vol. 98, p. 183101, May 2 2011.

[116] M. D. Ward and D. A. Buttry, "Insitu Interfacial Mass Detection with Piezoelectric Transducers," *Science,* vol. 249, pp. 1000-1007, Aug 31 1990.

[117] V. E. Bottom, *Introduction to quartz crystal unit design*. New York: Van Nostrand Reinhold, 1982.

[118] D. M. Ullevig, J. F. Evans, and M. G. Albrecht, "Effects of Stressed Materials on the Radial Sensitivity Function of a Quartz Crystal Microbalance," *Analytical Chemistry,* vol. 54, pp. 2341-2343, 1982.

[119] J. R. Barker, *Mechanical and electrical vibrations*. London, New York,: Methuen; Wiley, 1964.

[120] M. D. Ward, "Probing electrocrystallization of charge transfer salts with the quartz crystal microbalance," *Journal of Electroanalytical Chemistry,* vol. 273, pp. 79-105, 1989.

[121] J. Siegel, O. Lyutakov, V. Rybka, Z. Kolska, and V. Svorcik, "Properties of gold nanostructures sputtered on glass," *Nanoscale Research Letters*, vol. 6, 2011.